Dean Vortex Instabilities for Tubular Membrane Module Design (Second Year Final Progress Report)

(Agreement No. MRDP 699-501-94)

by
Georges Belfort, PI
Hanuman Mallubhotla
Meike Schmidt
and Johan Vente

Final Progress Report for the Second Year
(for the period April 1, 1995 to March 31, 1996)
April 20, 1996

Dean Vortex Instabilities for Tubular Membrane Module Design

Project # MRDP 699-501-94
RPI Fund # A70418

Georges Belfort, PI
Hanuman Mallubhotla, Graduate Student
Meike Schmidt, Graduate Student
Johan Vente, Graduate Student

Abstract

During the second year of this three-year grant, (i) we have reproduced the results obtained earlier, (ii) performed experiments at the same energy consumption levels for both helical and linear modules, (iii) determined the effects of flow rate, pH, solute concentration, type of solute, transmembrane pressure and energy consumption on the performance of both devices, and (iv) conducted Magnetic Resonance Imaging studies in curved glass tubes.

Pure water permeabilities were the same for both modules. Significant flux enhancements were obtained for the helical nanofiltration modules for all salt solutions under all test conditions, with little or no decrease in rejection. Salt fluxes were slightly higher for the helical module than the linear module.

Velocity contour profiles within Dean vortices produced by flowing water in solid-walled curved U tubes, were quantitatively measured, using Magnetic Resonance Imaging. Transverse shear rates (over and above the normal shear rates due to bulk axial flow) were measured at the walls of the tubes as functions of increasing flow rates, for several tubes of varying curvatures. Such shear rates increased with increasing flow rate. Increased shear rates of up to 350 % over that due to bulk flow were found. Bifurcation/twisting of vortices with increasing flow rate were also confirmed. The Dean number at which such bifurcation occurred was found to be a function of the curvature.

I. Introduction.

The presence of Dean vortices was shown to be effective in reducing concentration polarization and improving membrane performance [1]. Tests have been conducted in a helical nanofiltration module, built according to

our theoretical specifications, and compared to a conventional linear hollow fiber module. Improvements of up to 55 % for salt solutions and 100 % for salt and silica suspensions were observed on a similar flow rate basis.

The main goal for the fourth quarter of the second year of this project was to conduct MRI experiments in curved glass tubes with different curvatures. The results reported here summarize our previous quarterly reports [2-4] together with additional new results and are presented below.

II. Methods and materials.

The construction and operation of the helical and linear hollow fiber modules were described previously [1]. The MRI system is described briefly below.

Water doped with cupric sulfate to reduce the relaxation times, was pumped into a glass tube placed horizontally inside a 2 Tesla superconducting magnet, by means of a centrifugal pump (Figure 1). The flow through the U tube was controlled by valves in the recycle and bypass lines, and was measured by a rotameter. Two and three dimensional NMR pulse sequences were used to measure flow in the U tube.

Figure 2 shows the two-dimensional pulse sequence with flow encoding gradients before and after the 180^0 rf-pulse. Spins in the sample have their phase shifted by the first gradient during the period *flowt* before the 180^0 pulse. Spins which have not moved have the phase shift undone by the second velocity-encoding lobe in the *flowt* period after the 180^0 pulse. Spins in fluid with a velocity in the z direction will experience a different phase shift in the second gradient lobe than was produced by the first lobe, so their net phase angle differs from the phase angle of spins which did not move.

For a constant longitudinal velocity, the phase change ($\Delta\phi$) for a moving spin is proportional to the product of the first moment of the field gradient (G) and the velocity (V) as:

$$\Delta\phi = \gamma V \int tG(t)dt \qquad (1)$$

where γ is the gyromagnetic ratio and t is the time. The other gradients in the sequence are used to obtain spatial information for imaging.

A three dimensional pulse sequence applies encoding gradients in steps, giving two dimensions of spatial information and one dimension of velocity information (Figure 3). Because of their small amplitudes compared to the longitudinal velocity, three dimensional pulse sequences were required for the measurement of transverse velocities. A more detailed description of these methods is already published [5]. To calibrate the MRI system, the phase change $\Delta\phi$ for a given mean longitudinal velocity was obtained as a function of magnetic gradient. The phase shift offset was then removed by averaging

the phase shift of the same positive and negative gradients. The theoretical slope obtained from Eq. 1 is compared to the experimental data in Figure 4.

III. Results and Discussion.

Nanofiltration.

During the first quarter of the second year, several problems were encountered. The older modules were fouled after prolonged usage and many of the hollow fibers leaked, while the new modules had imperfect fibers and unacceptable water permeabilities. The manufacturing process at Bend Research changed within the past year and had caused some of these difficulties. Methods of testing the integrity of the hollow fiber modules and the proper way of calculation of the average transmembrane pressure for the helical module were established during this period. For every set of modules, permeability tests with pure water and rejection tests with $MgSO_4$ solutions were conducted prior to other experimentation.

Various operating variables are discussed below with respect to their influence on the performance of the NF modules.

Axial pressure drop and friction coefficient.

It has been shown previously that excellent agreement was obtained for axial pressure drop measurements with the theory of Ito [2, 6]. Axial pressure drops for both helical and linear modules were also measured under various test conditions. These included (a) pure water without permeate flow, (b) pure water with permeate flow, and (c) aqueous $MgSO_4$ solutions at various transmembrane pressures. An experimentally obtained correlation for λ_h, the friction coefficient in a helical system and laminar flow was given by Mishra and Gupta [7]:

$$\frac{\lambda_h}{\lambda_s} = 1 + 0.033 \left(\log_{10} De\right)^{4.0} \qquad De < 3000 \qquad (2)$$

Measured axial pressure drops are shown in Figure 5 (a), (b), (c) and (d). Power law equations fitted to the data showed very little variation.

Calculated friction factors are compared to those calculated using Eq. 2 in Figure 6 (a), (b) and (c). Excellent agreements were obtained for all cases tested. These results clearly demonstrate that solvent permeation, solute concentration and transmembrane pressure do not affect the axial pressure drop and hence, energy consumption levels. This is important for design and scale up considerations.

Water permeability and pH.

The water permeabilities were measured after every series of experiments in order to ascertain the integrity of the modules and were found to be very close for the helical and linear modules in all cases (Figure 7 (a)).

Water permeability tests were performed at various pH values to determine the effect of changing pH. The pH was adjusted by adding small

amounts of monovalent acid (HCl) and base (NaOH). As shown in Figure 7 (b), there was no significant effect of pH on the water permeability (slope) of either module. The observed change in fluxes of salt solutions is therefore attributed to the changing behavior of the solute species and its interaction with the membrane at different pH values.

Solute concentration and transmembrane pressure.

The absolute permeabilities of both modules decreased with increasing solute concentration. However, the improvement in permeability in the presence and absence of Dean vortices increased with increasing concentration (Figure 8 (a) and (b)). Increasing transmembrane pressure improved performance. Figures 9 (a) and (b) show the permeabilities at various energy consumptions at two different transmembrane pressures. At larger transmembrane pressures, the effectiveness of vortices in reducing concentration polarization was much stronger than at lower transmembrane pressures.

The effects of solute concentration and transmembrane pressure are connected with the effects of other variables and can be seen more clearly in the following sections.

Soulte type.

Permeabilities and rejections of aqueous solutions of three salts of different valencies (KCl, K_2SO_4 and K_3PO_4) are shown in Figure 10 (a) and (b). The higher permeability for the K_3PO_4 solution was probably due to the high pH, while the formation of a complex monovalent ion ($KHPO_4^-$) is suspected to be the cause of lower rejection [3].

Effect of flow rate and energy consumption.

As can be seen from Figure 9 (a) and (b), increasing flow rate generally caused an increase in flux improvement. Figures 11 -14 show the permeation flux as a function of the energy consumption, E. For all concentrations of $MgSO_4$, increasing E increased the flux enhancement. Also, increasing transmembrane pressure had a beneficial effect. The same data were converted to permeabilities and plotted in Figures 15 - 17. Note that even though the fluxes were normalized by the net driving force ($\Delta p - \sigma\Delta\pi$), the improvement in permeability increased with increasing E as well as with increasing transmembrane pressure. The permeabilities of the helical module increased, while those of the linear module remained nearly the same. This is because increasing E has a non-linear effect on permeability improvement, resulting in a non-linear increase in permeability enhancement with increasing transmembrane pressure.

Rejection and solute flux.

The rejection of the helical module was slightly lower than that of the linear module for all cases tested. The solute flux was consequently higher for the helical module. Figure 18 (a) and (b) show the rejection and solute flux as functions of increasing concentration, respectively.

The observed rejections are plotted as functions of the Dean number ratios in Figure 19 (a) - (d). The rejections increased with increasing flow rate

or Dean number for both helical and linear modules. For all concentrations of $MgSO_4$, the rejections of the helical module increased with increasing transmembrane pressure, while the rejections of the linear module remained nearly the same. Changing concentration of $MgSO_4$ did not have a significant effect on R_{obs}. Solute fluxes changed significantly, however, with changing concentration (Figure 20), while the change was not as pronounced for changing transmembrane pressure at a given concentration (Figure 21 (a) - (d)).

Magnetic Resonance Imaging.

Typical velocity profiles in a curved tube are shown in Figure 22. The distortion of the contours is caused by the centrifugal on the left side of the figure. The velocity contours before the bend are parabolic profiles. No difference was seen between the axial velocity contours produced by the two and three dimensional pulse sequences as shown in Figure 23. Changes in the structure of the axial velocity contour plots for one tube are shown with changing flow rate or Dean number (De_C = 16.42) in Figure 24. The local velocity maximum is offset from the central axis because of the centrifugal force and becomes more pronounced with increasing flow rate. Also, it is affected by the structure of the vortices.

Transverse velocity or arrow plots of the vortices are shown in Figure 25 for the same tube, at the same flow rates. Increasing flow rate caused twisting or bifurcation of the vortex structure. At the highest flow rates tested for this tube, up to six vortices have been found (Figure 26).

Similar results were obtained for five different tubes. Transverse shear rates (γ_t) at the walls were estimated in the region shown in Figure 26. These shear rates (divided by the bulk axial shear rate) are plotted as a function of Dean number for different radius ratios of the tubes (Figure 27). The radius ratio is defined as a/r_C, where a is the radius of the tube and r_C is the radius of curvature. The shear rates increased with increasing radius ratio or increasing curvature ($1/r_C$). The "dip" behavior was observed for all tubes. These results support similar results obtained for nanofiltration (Figure 9 (a) and (b) - see arrows).

Conclusions.

The method of producing well-defined, Dean centrifugal instabilities was shown to have a beneficial effect on membrane performance in nanofiltration. Under all experimental conditions we have tested, the performance of the helical module was better than that of the linear nanofiltration module in terms of productivity. A slight loss of rejection was observed. Flux improvements of up to 30 % have been observed. This is in spite of the fact that we have operated at relatively low flow rates.

Detailed results concerning the effect Dean vortices on the permeation fluxes of nanofiltration membranes were obtained. The main conclusions are:

(1) No siginificant difference was found in the water permeabilities of both linear and helical modules. Changing pH had no effect on the water permeability of either module. The presence of Dean vortices was effective only when salt or foulants were present in the feed.

(2) Axial pressure drop and energy consumption measurements agreed very well with established correlations in literature. Permeation flux had no noticeable effect on the flow characterisitics of the system. Flux improvements in the helical module over the linear module of up to 30 % were observed at the same energy consumption levels. This improvement increased with increasing energy consumption. Operating at even higher energy consumptions would be advantageous.

(3) For the nanofiltration of $MgSO_4$ solutions, the flux improvement increased with transmembrane pressure and concentration for both cases of constant flow rate [1] and constant energy expenditure experiments.

(4) Rejections of the $MgSO_4$ solutions were slightly lower and solute fluxes higher for the helical module than the linear module.

(5) Effects of the valency of the inorganic salts and the solution pH were found to be interconnected. The flux increased at high pH, probably due to the dissolution of the active layer.

(6) Transverse velocities and increased shear rates induced by Dean vortices have been measured by MRI. Twisting and bifurcation of vortex structure with increasing flow rate was confirmed. Up to six vortices were found. Increasing Dean number caused increasing transverse shear rate over that of the bulk flow. Transverse shear rates of up to 350 % over that due to bulk flow were obtained suggesting significant potential flux improvements at higher flow rates.

In general, we have shown that operating with Dean vortices at higher flow rates, energy consumptions, transmembrane pressures and concentrations is advantageous.

Patent.

A US patent was applied for in August 1995. We are currently responding to the examiner's rejection.

Future Work.

The objectives for the third and final year of this project are described below.

1. Long-term experiments at high concentrations will be performed.

2. Nanofiltration of other salts will be performed. Ions such as Na^{+}, Mg^{++} and Ca^{++} will be mixed and the effectiveness of Dean vortices on the separation of these ions will be determined.
3. Magnetic Resonance Imaging. We have conducted MRI studies for laminar flow in a 180° curved tube. Next, we plan to conduct MRI experiments in helical glass tubes to understand the performance of the helical tubular membrane. Effect of the presence of particles will also be studied.
4. Numerical Solutions. Using the software Fluent, the N-S equations will be solved to confirm MRI experimental findings. Convective-diffusion equations for fast Dean flows with variable wall flux and variable parameter properties will also be solved.

Acknowledgments.

We would like to thank Dr. Rod Ray and Dr. Scott McCray of Bend Research, Oregon for their continuing support in constructing the membrane modules according to our theoretical specifications. We are grateful to Dr. William Edelstein and Dr. Thomas Early for assisting us with the MRI experiments and General Electric Company for allowing us to use the MRI facility. We would also like to acknowledge Mr. Sven Hofmann's help in constructing the nanofiltration system.

References.

1. Belfort, G., Mallubhotla, H., Hofmann, S., Final Project Report to NWRI, # MRDP-699-501-94, January 1995.
2. Belfort, G., Mallubhotla, H., Schmidt, M., First Quarterly Report to NWRI, August 1995.
3. Belfort, G., Mallubhotla, H., Schmidt, M., Second Quarterly Report to NWRI, September 1995.
4. Belfort, G., Mallubhotla, H., Vente, J., Third Quarterly Report to NWRI, January 1996.
5. Chung, K-Y., Edelstein, W. A., Li, X., Belfort, G., AIChE Journal, 39, 1592, 1993.
6. Ito, H., Zeitschrift fur angewandte Mathematik und Mechanik, 49, 653, 1969.
7. Mishra, P., Gupta, S., Ind. Engg. Chem. Proc. Des. Dev., 18, 130, 1979.

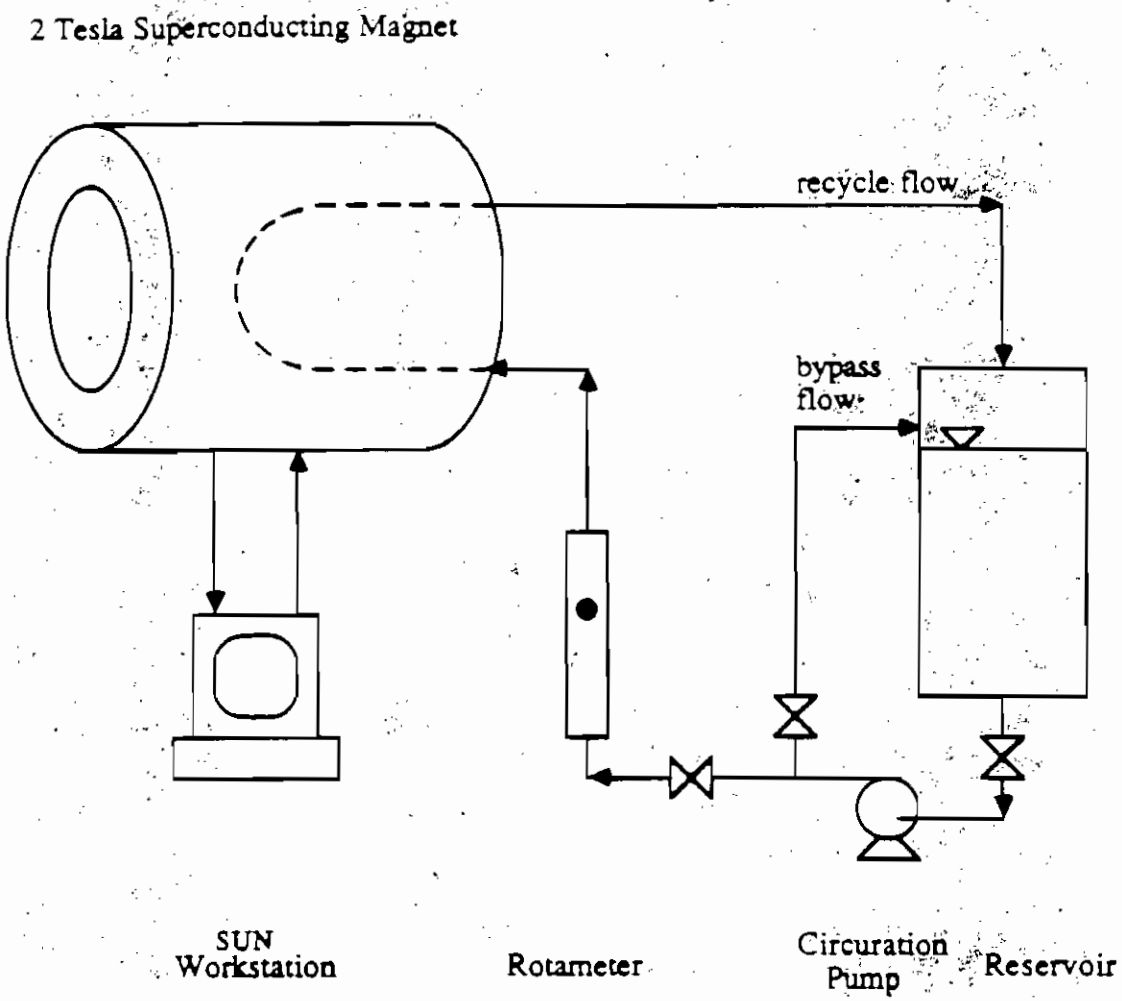

Fig. 1. Magnetic Resonance Imaging system.

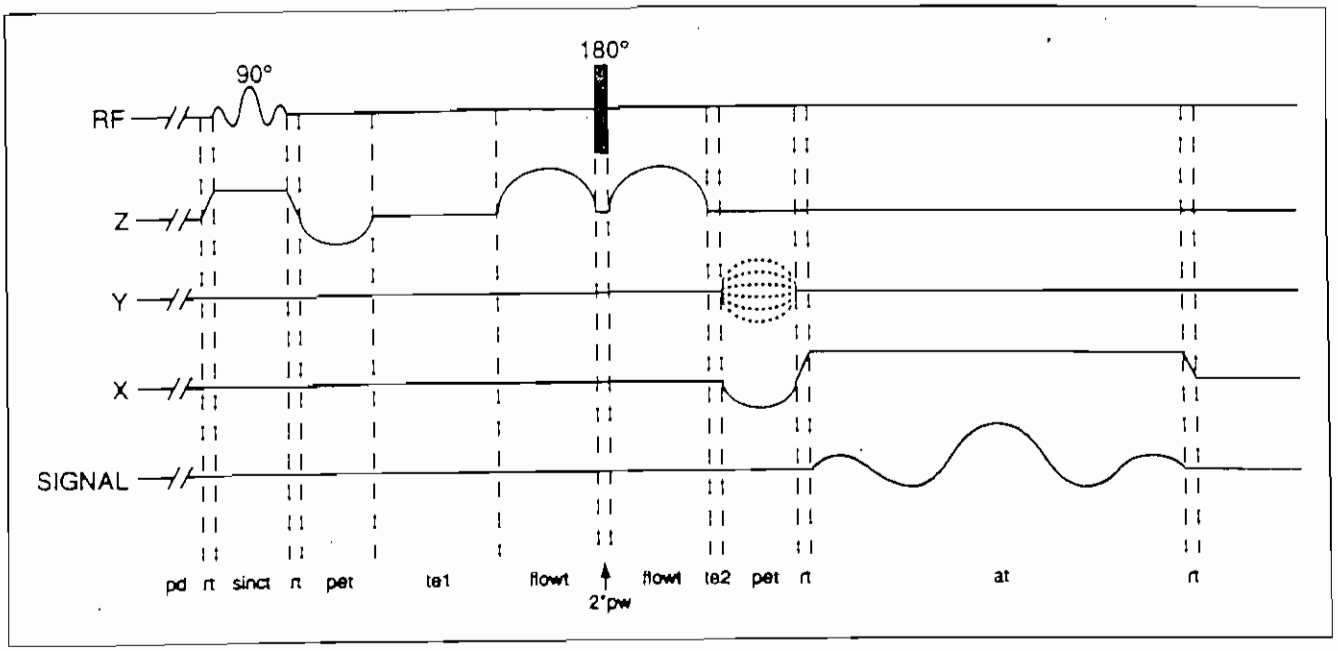

Figure 2. Two-dimensional flow NMR pulse sequence.

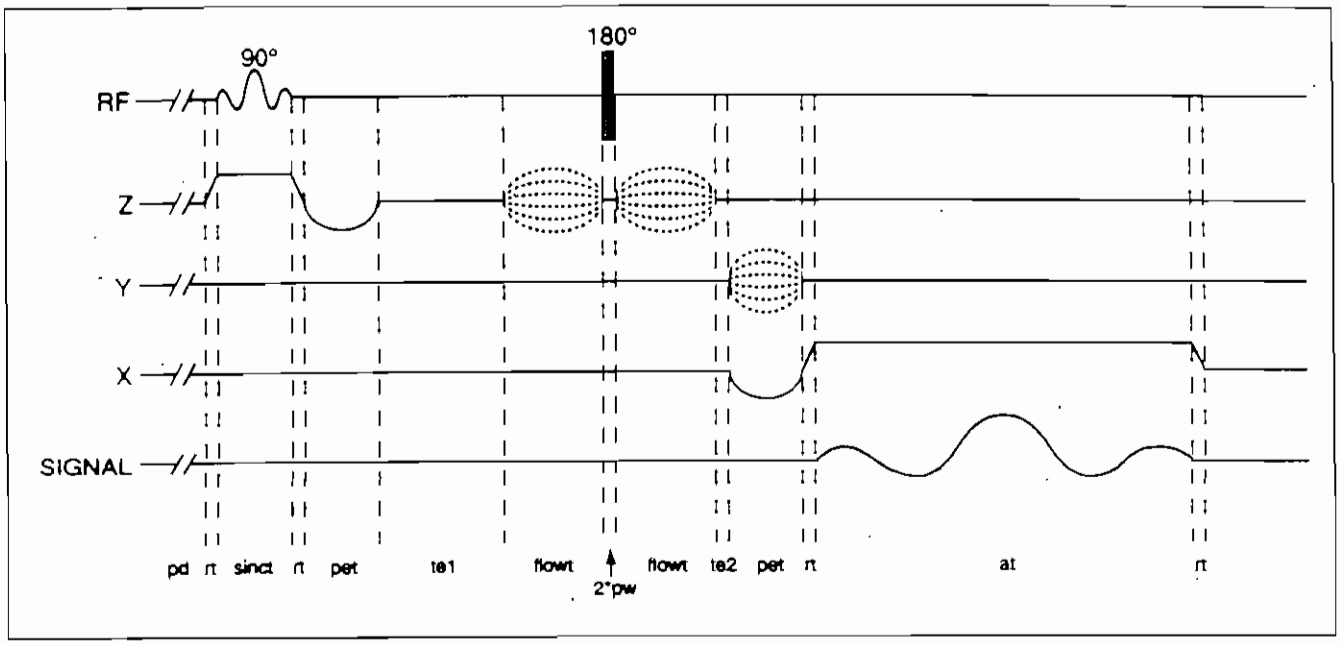

Figure 3. Three-dimensional flow NMR pulse sequence.

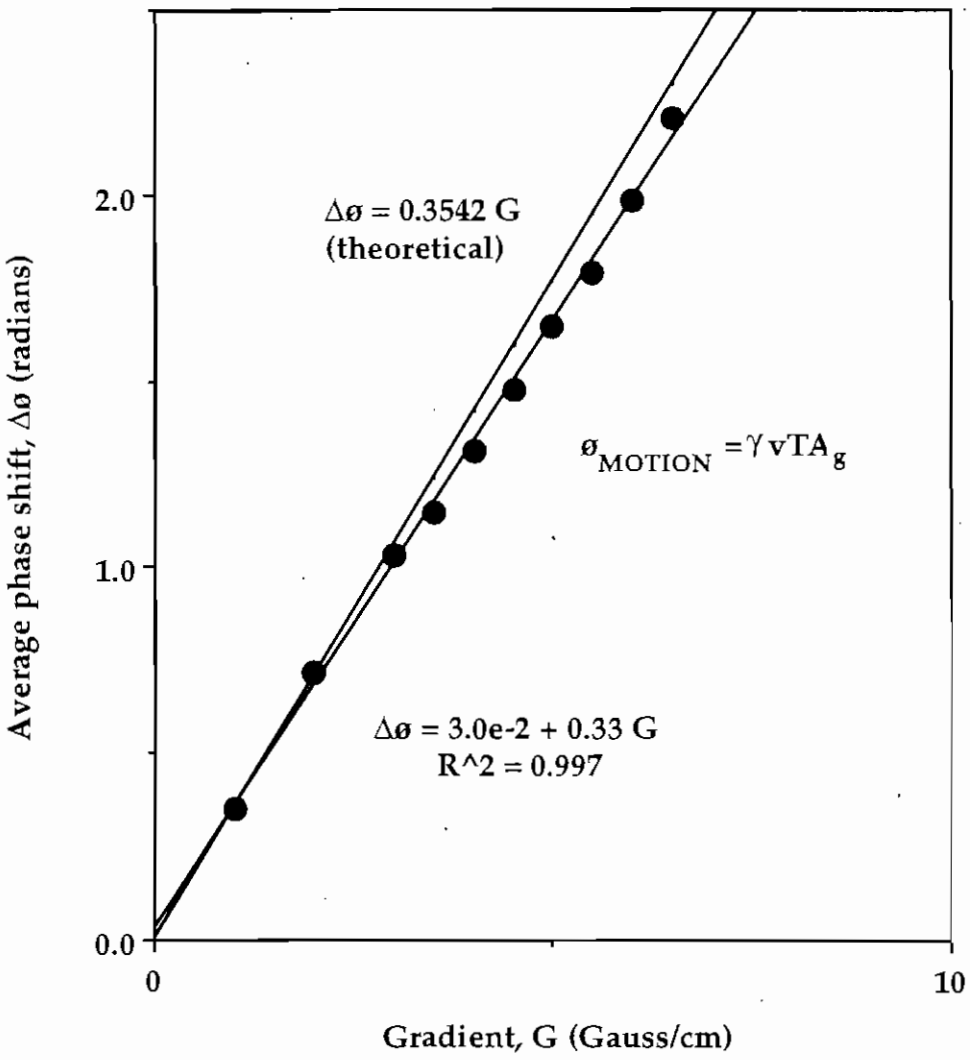

Fig. 4. Theoretical vs. averaged experimental phase shift $\Delta\phi$ as a function of flow gradient strength G at a flow rate Q = 120 ml/min.

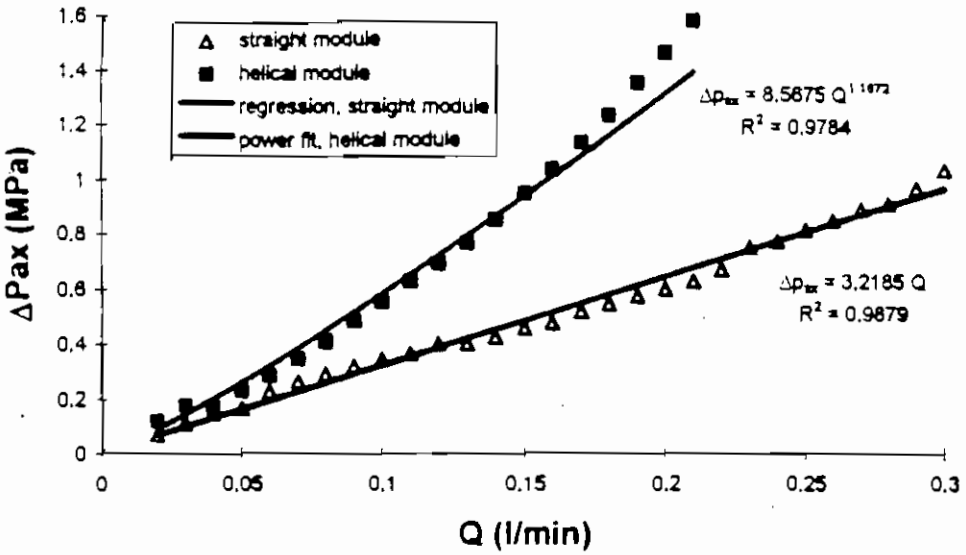

Fig. 5 (a). Axial pressure drop as a function of flow rate for pure water (without permeate flow).

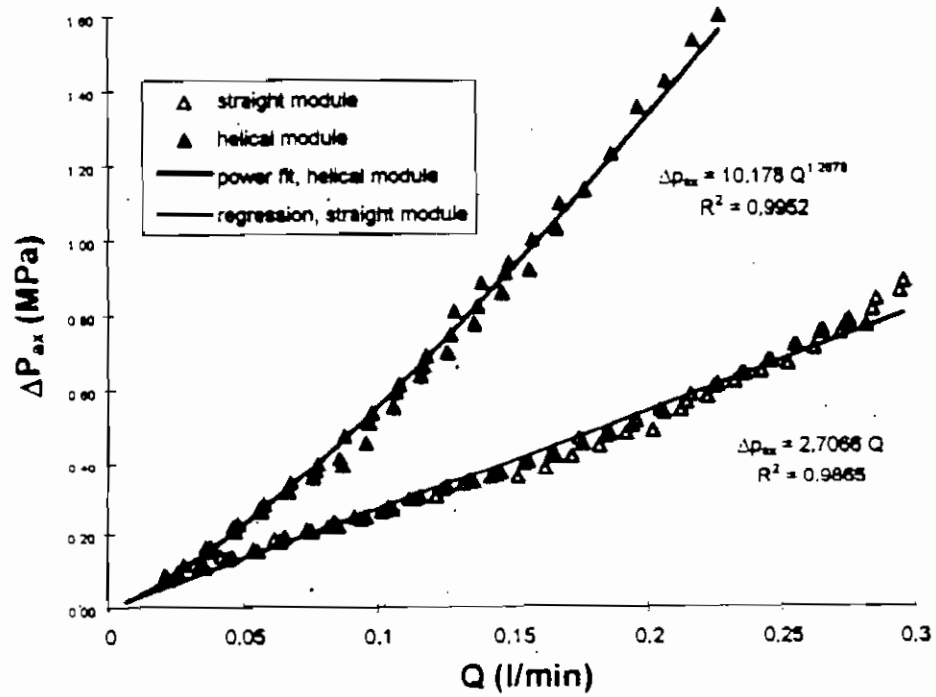

Fig. 5 (b). Axial pressure drop as a function of flow rate for pure water (with permeate flow).

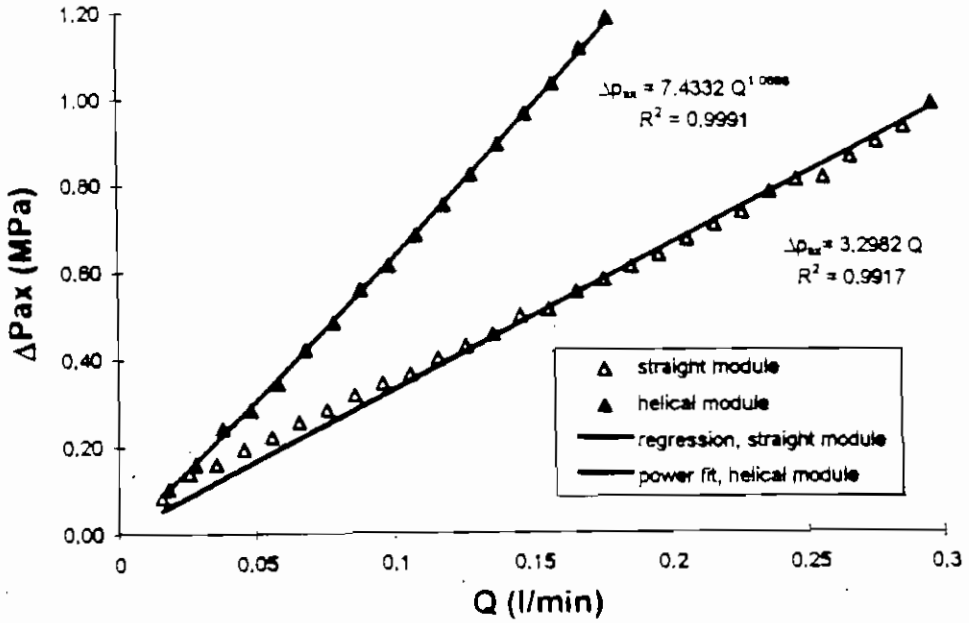

Fig. 5 (c). Axial pressure drop as a function of flow rate for $MgSO_4$ solution (with permeate flow). TMP = 1.0 Mpa, c = 2000 ppm.

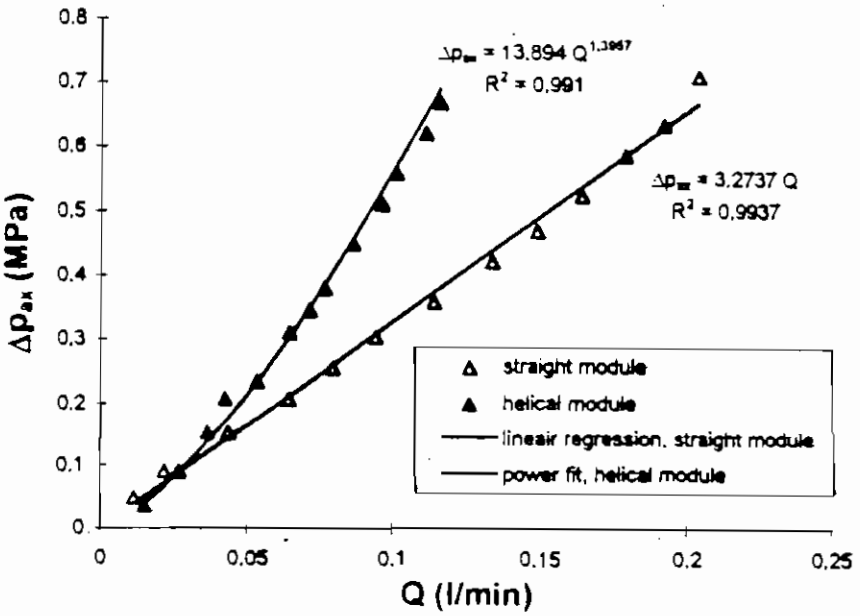

Fig. 5 (d). Axial pressure drop as a function of flow rate for $MgSO_4$ solution (with permeate flow). TMP = 1.4 Mpa, c = 2000 ppm.

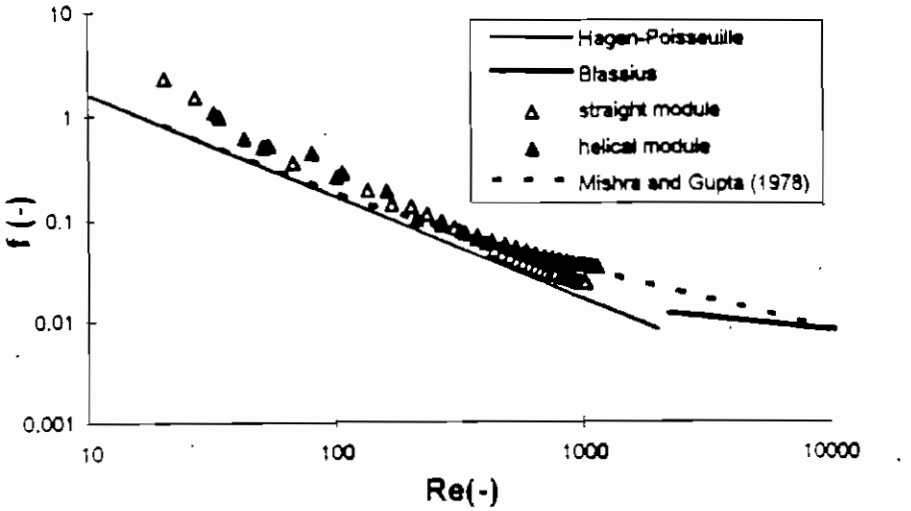

Fig, 6 (a). Friction factor as a function of Reynolds number for pure water (without permeate flow).

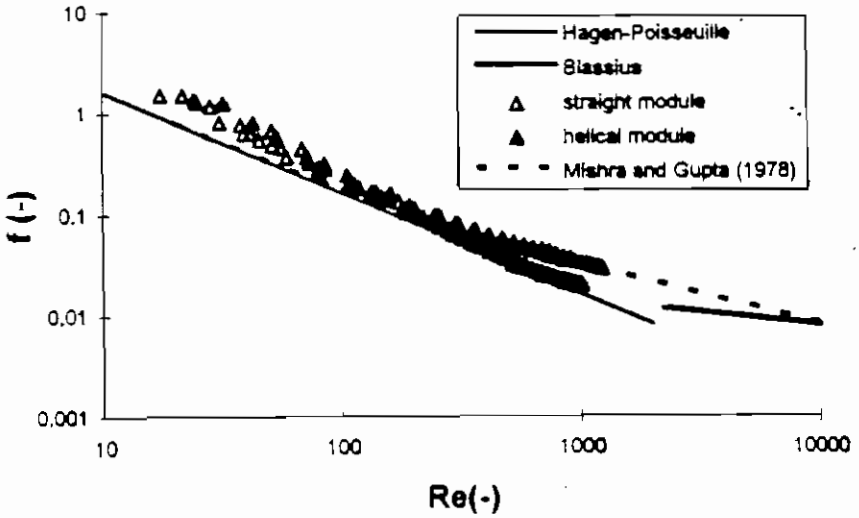

Fig, 6 (b). Friction factor as a function of Reynolds number for pure water (with permeate flow).

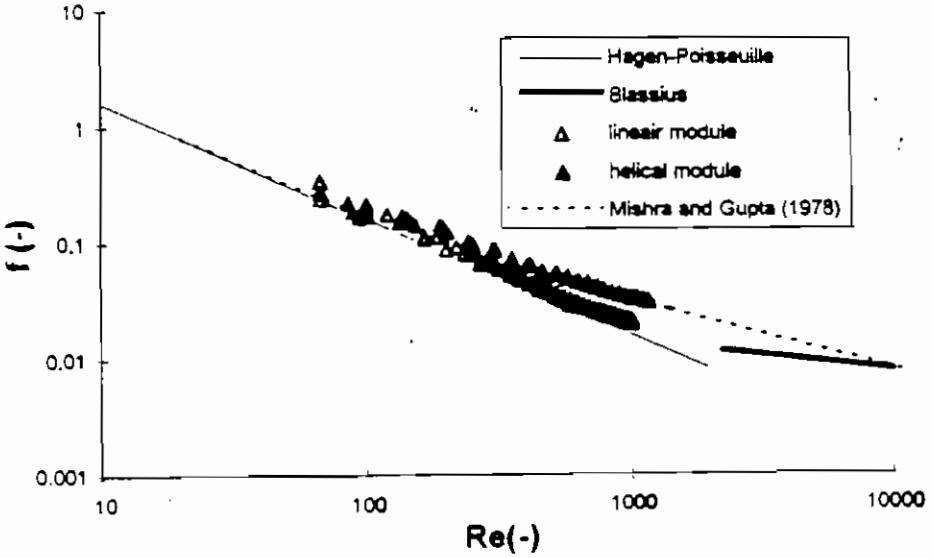

Fig, 6 (c). Friction factor as a function of Reynolds number for $MgSO_4$ solution (with permeate flow). TMP = 1.0 Mpa, c= 2400 ppm.

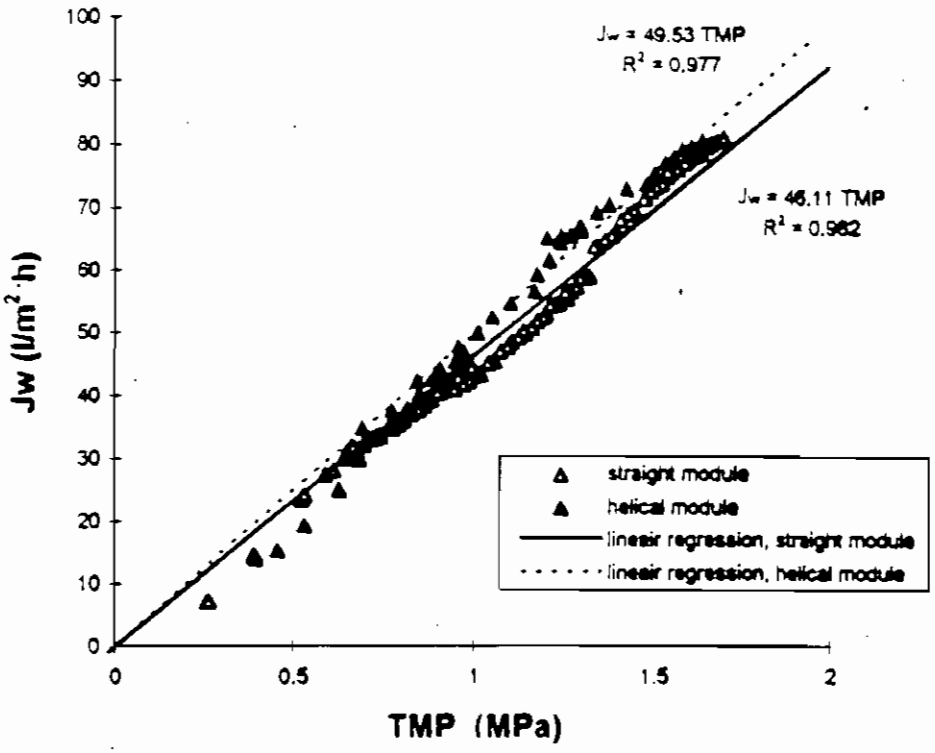

Fig. 7 (a) Pure water permeabilities for the nanofiltration modules. pH = 5.7, T = 300 K.

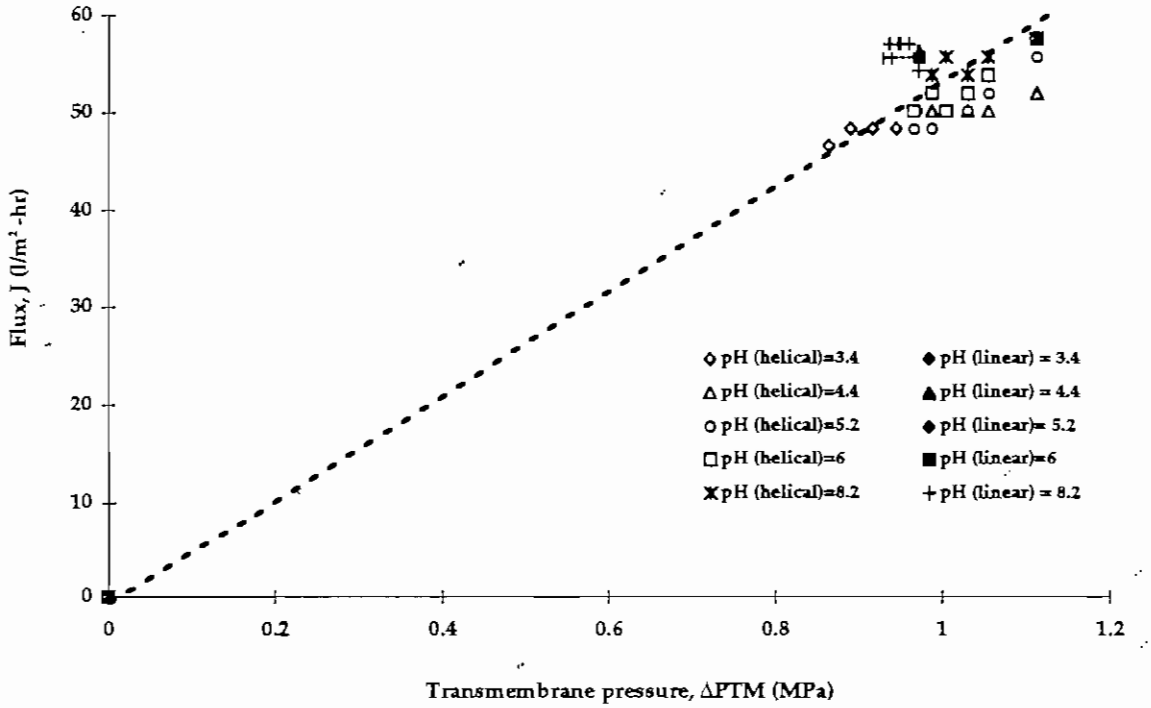

Fig. 7 (b) Effect of pH on water permeability. The dashed line is in place of the data from Fig. 7 (a).

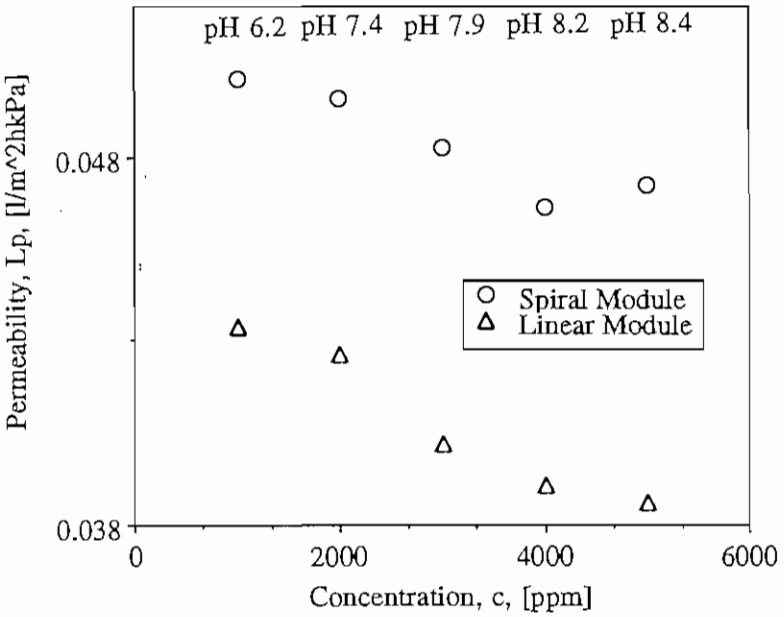

Fig. 8 (a). Average permeability versus concentration for aqueous $MgSO_4$ solutions. TMP = 1400 kPa, T = 297 K, E = 88 W/m^2.

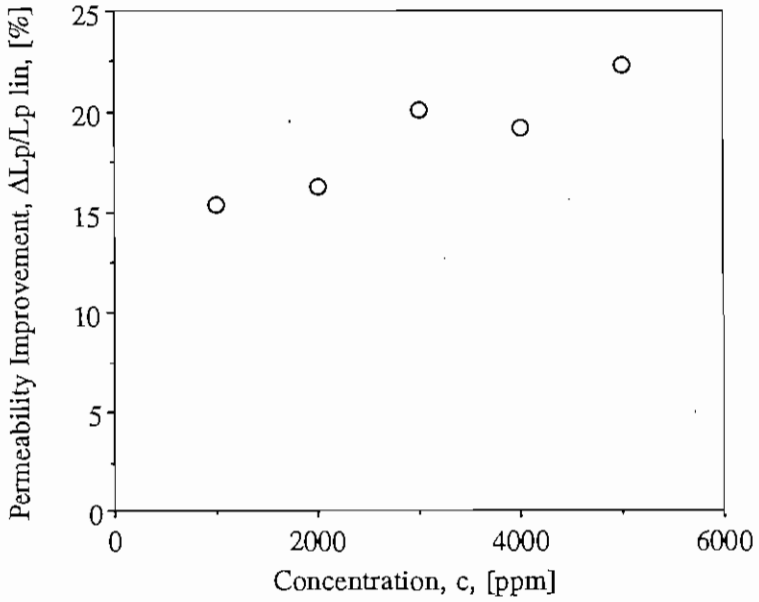

Fig. 8 (b). Permeability improvement versus concentration for aqueous $MgSC_4$ solutions. TMP = 1400 kPa, T = 297 K, E = 88 W/m^2.

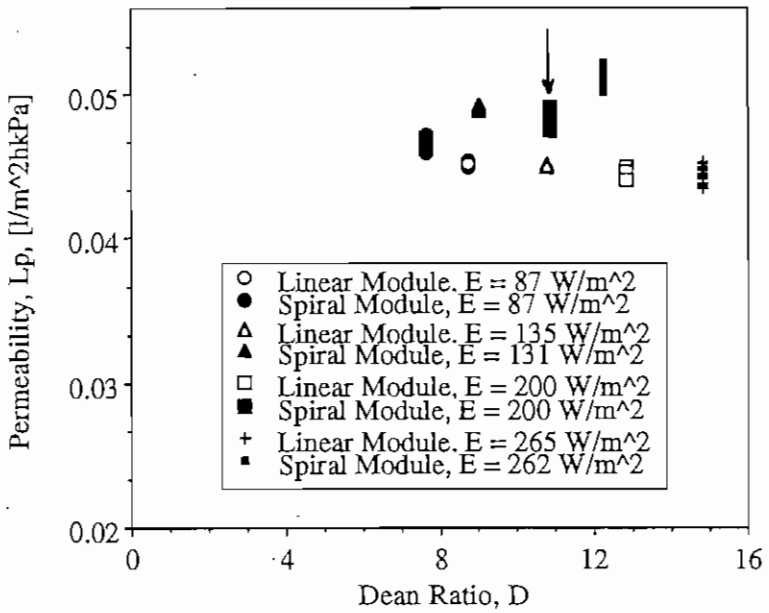

Fig. 9 (a). Permeability versus Dean number ratio for aqueous $MgSO_4$ solutions. c = 2000 ppm, TMP = 1000 kPa, T = 297 K, pH = 7.4. All data points from Figure 1 are plotted.

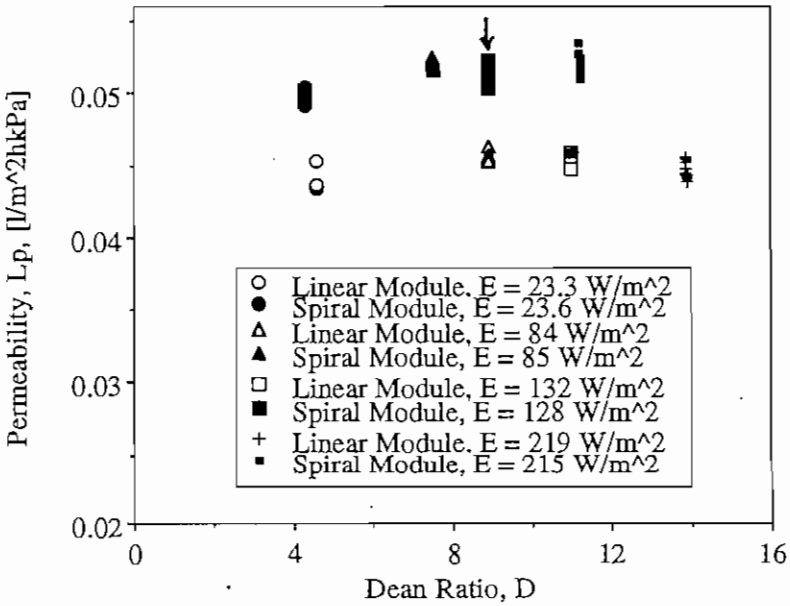

Fig. 9 (b). Permeability versus Dean ratio for aqueous $MgSO_4$ solutions. c = 2000 ppm, TMP = 1400 kPa, T = 297 K, pH = 7.4. All data points from Figure 3 are plotted.

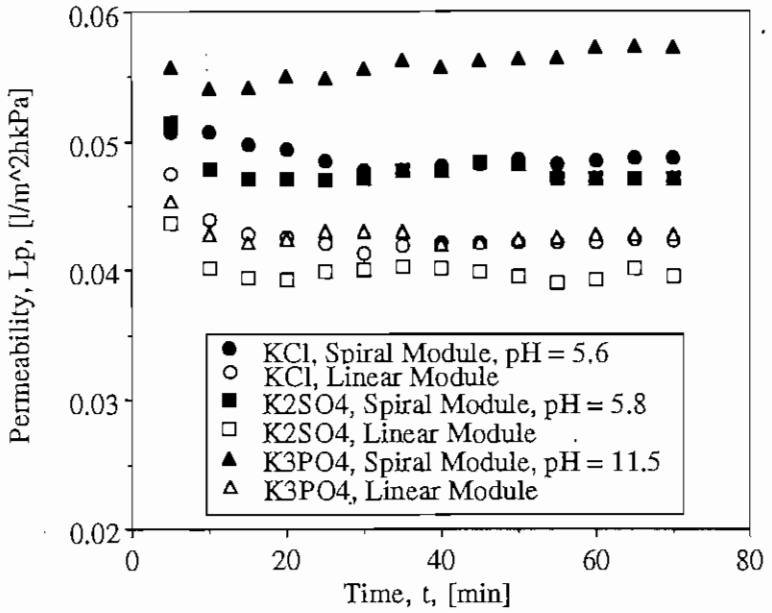

Fig. 10 (a). Permeability versus time for the aqueous solutions of three different salts. c = 0.02 mol/l, TMP =1400 kPa, T = 297 K, D = 7.5.

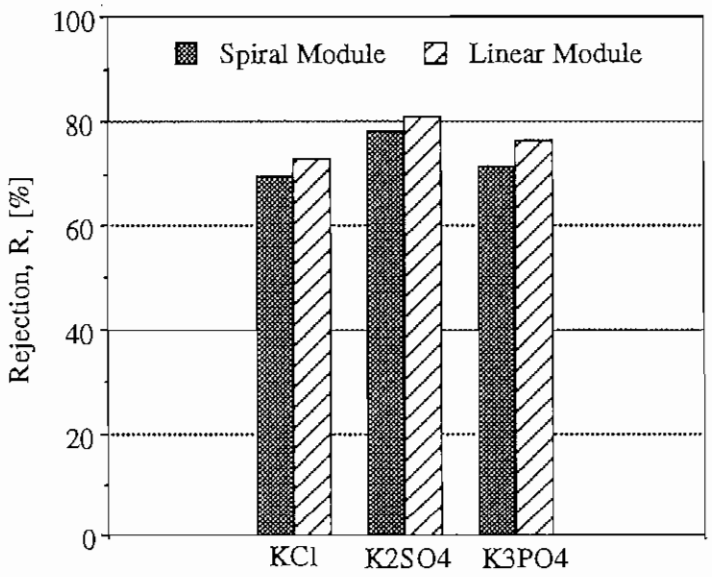

Fig. 10 (b). Rejection of aqueous solutions of three different salts. c = 0.02 mol/l, TMP = 1400 kPa, T = 297 K, D = 7.5.

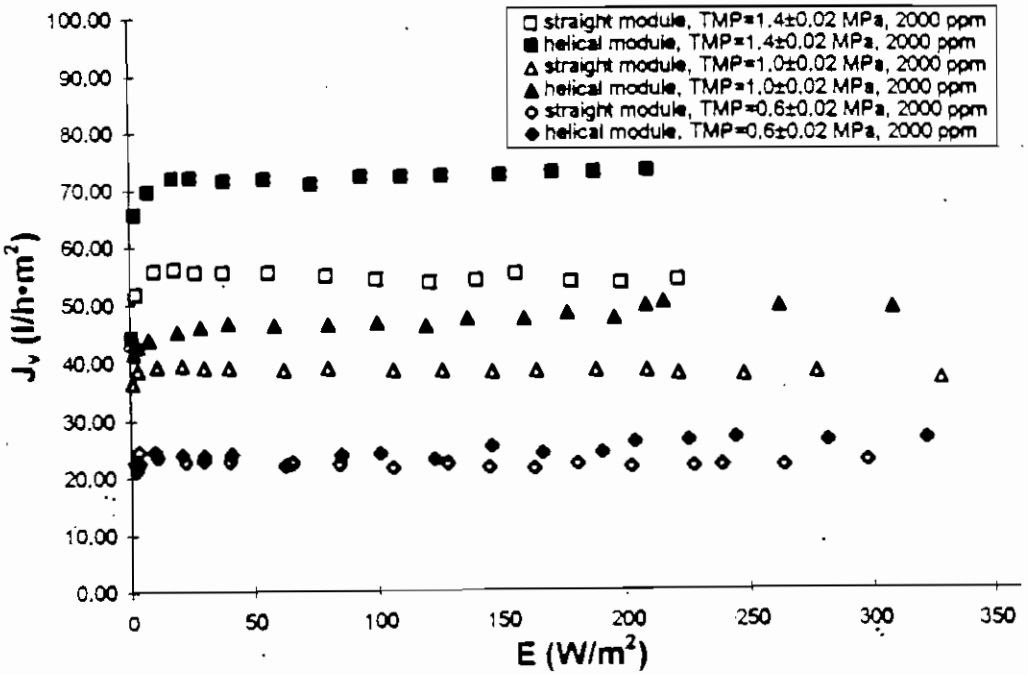

Fig, 11. Permeation flux as a function of energy consumption for 2000 ppm $MgSO_4$ solution, at pH = 6.3.

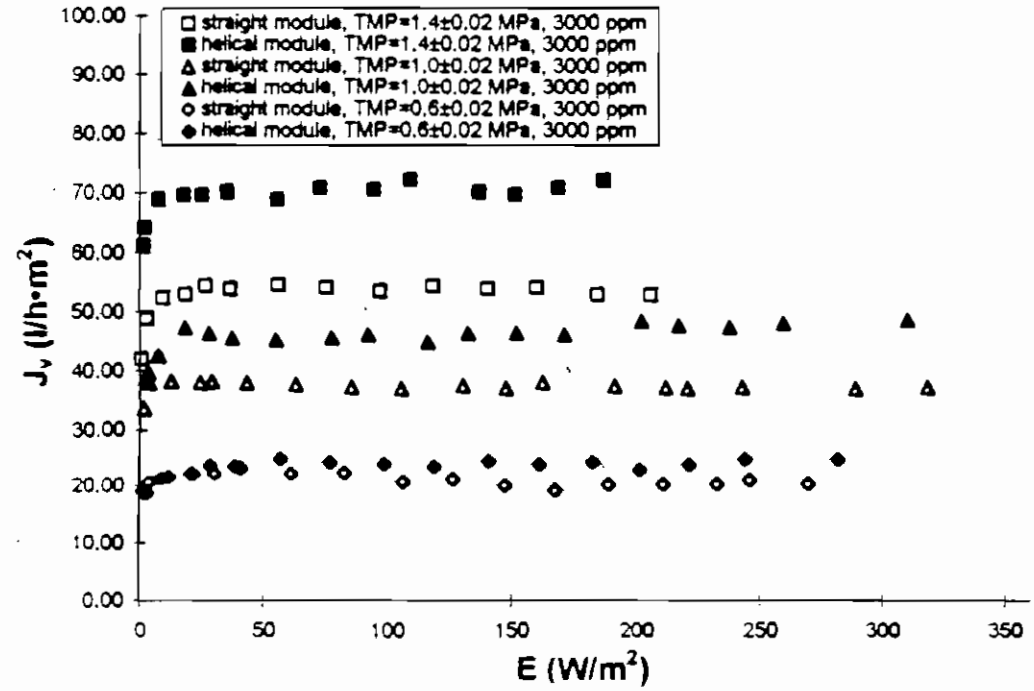

Fig, 12. Permeation flux as a function of energy consumption for 3000 ppm $MgSO_4$ solution, at pH = 6.3.

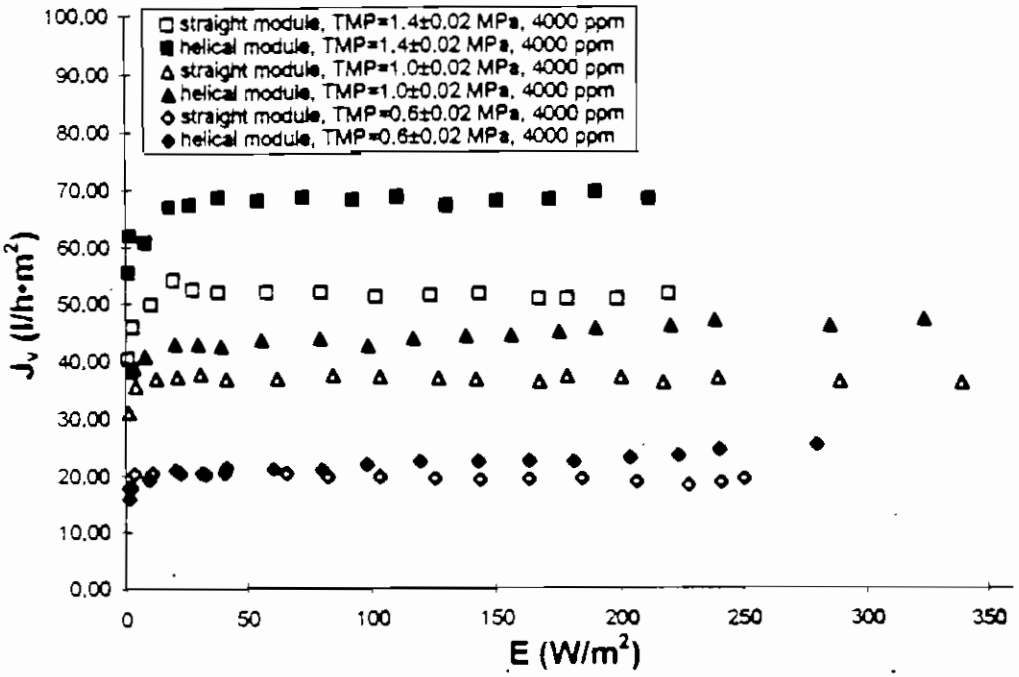

Fig, 13. Permeation flux as a function of energy consumption for 4000 ppm $MgSO_4$ solution, at pH = 6.3.

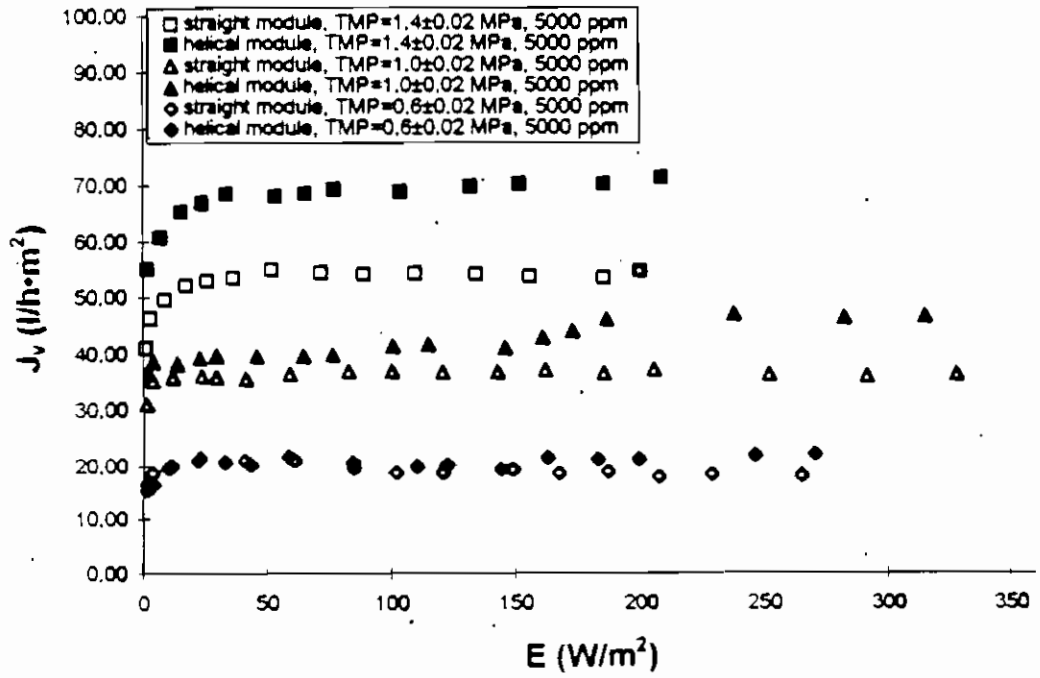

Fig, 14. Permeation flux as a function of energy consumption for 5000 ppm $MgSO_4$ solution, at pH = 6.3.

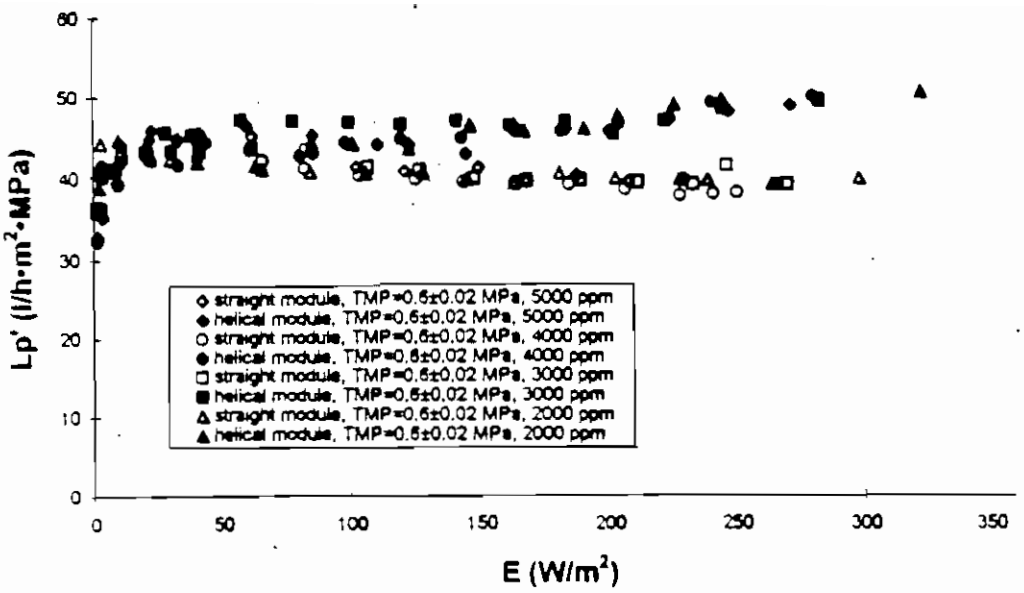

Fig. 15. Permeability as a function of energy consumption for TMP = 0.6 MPa.

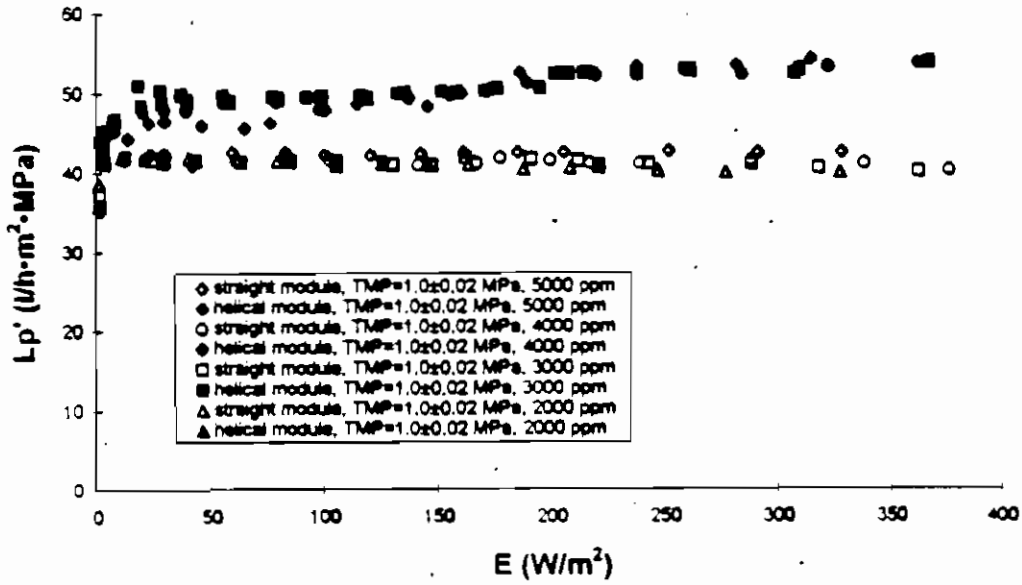

Fig. 16. Permeability as a function of energy consumption for TMP = 1.0 MPa.

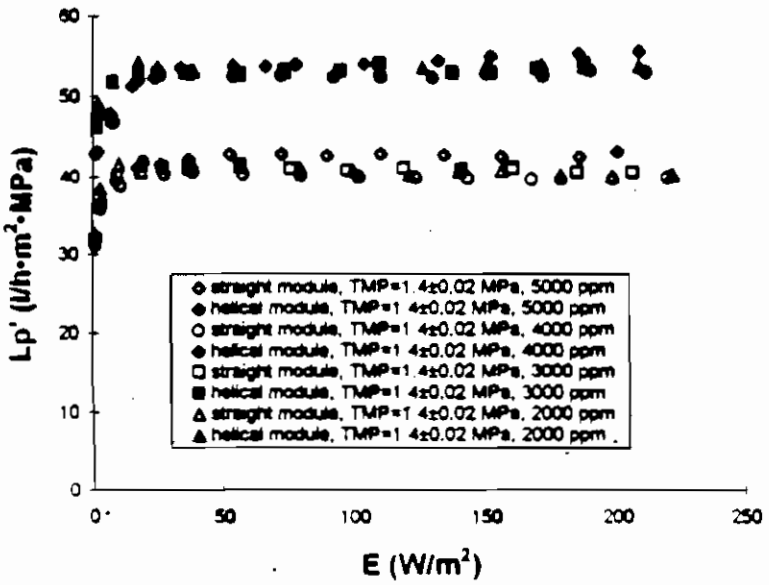

Fig. 17. Permeability as a function of energy consumption for TMP = 1.4 MPa.

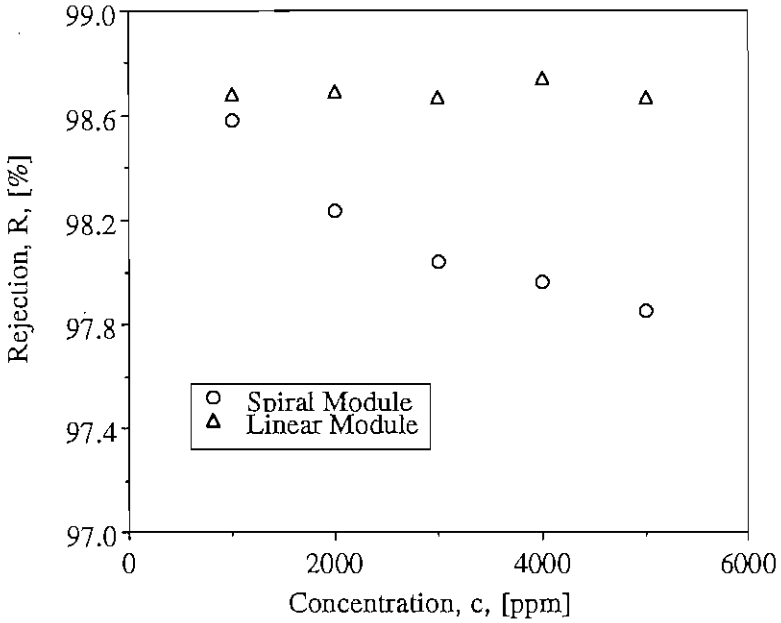

Fig. 18 (a). Rejection versus concentration for aqueous $MgSO_4$ solutions. TMP = 1400 kPa, T = 297 K, E = 88 W/m^2

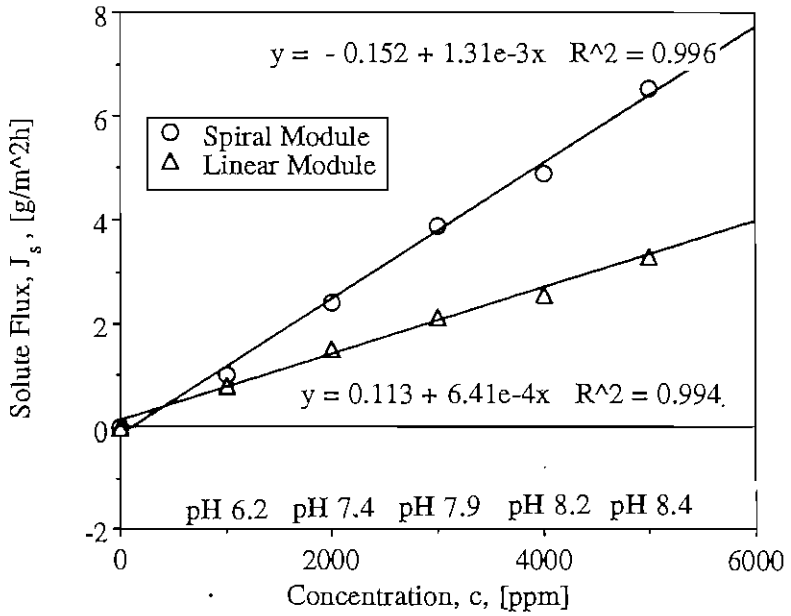

Fig. 18 (b). Solute flux versus feed concentration for aqueous $MgSO_4$ solutions. TMP = 1400 kPa, T = 297 K, E = 88 W/m^2.

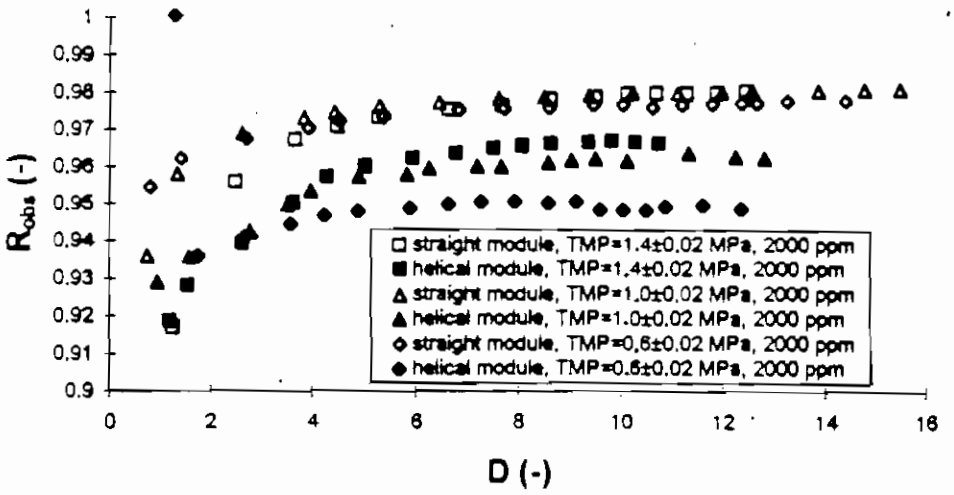

Fig. 19 (a) Observed rejection as a function of Dean number, 2000 ppm $MgSO_4$ solution, pH = 6.1.

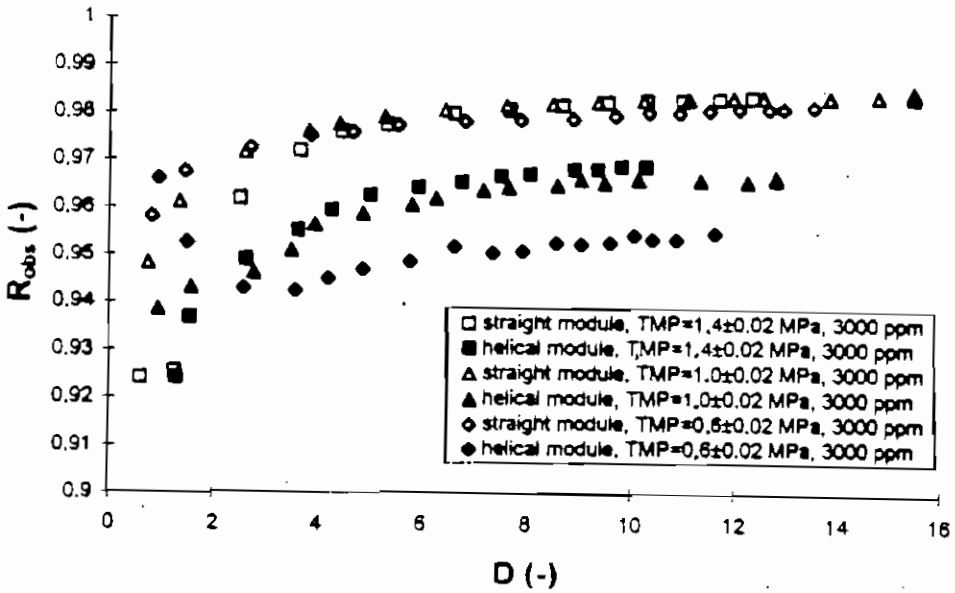

Fig. 19 (b) Observed rejection as a function of Dean number, 3000 ppm $MgSO_4$ solution, pH = 6.1.

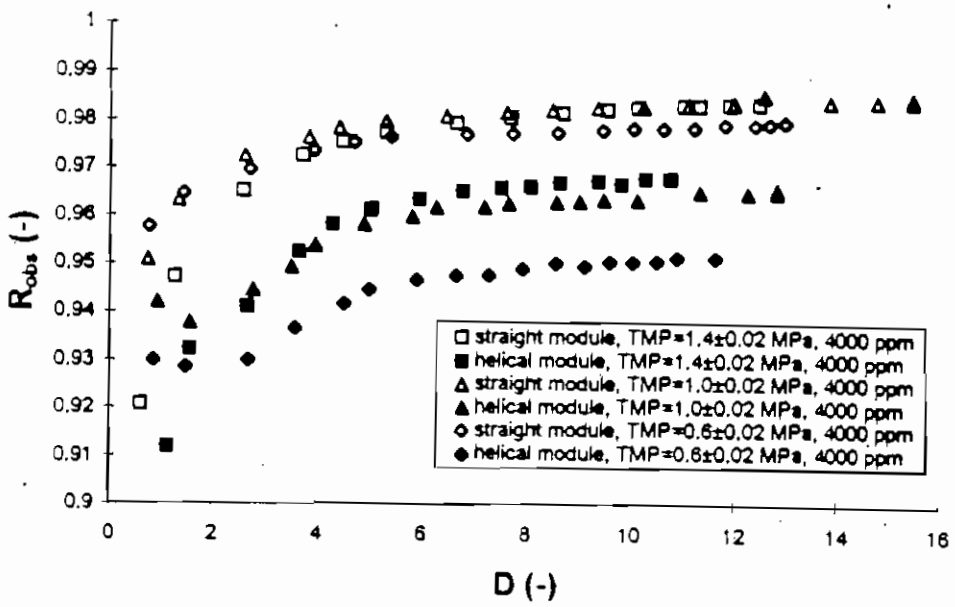

Fig. 19 (c) Observed rejection as a function of Dean number, 4000 ppm $MgSO_4$ solution, pH = 6.1.

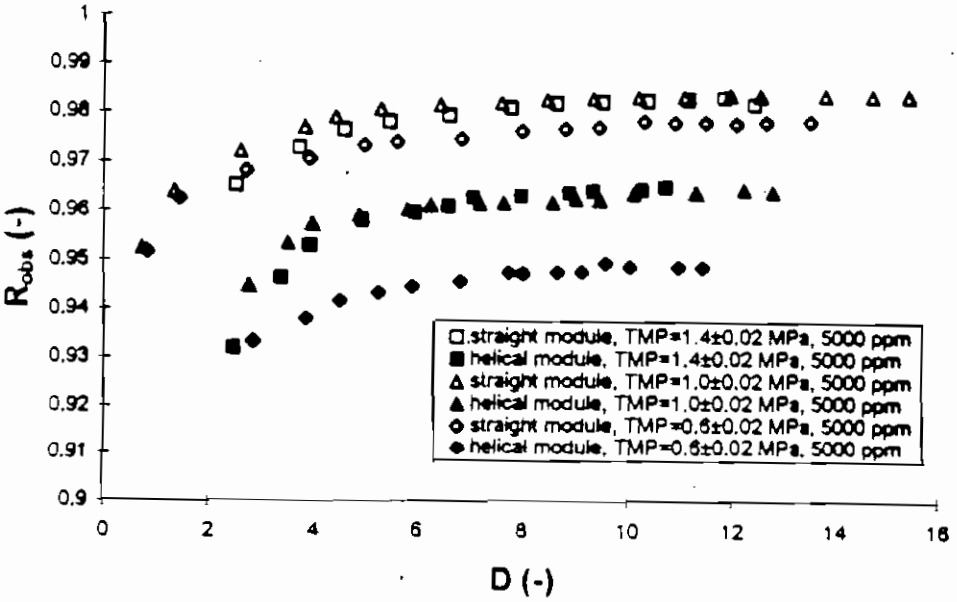

Fig. 19 (d) Observed rejection as a function of Dean number, 5000 ppm $MgSO_4$ solution, pH = 6.1.

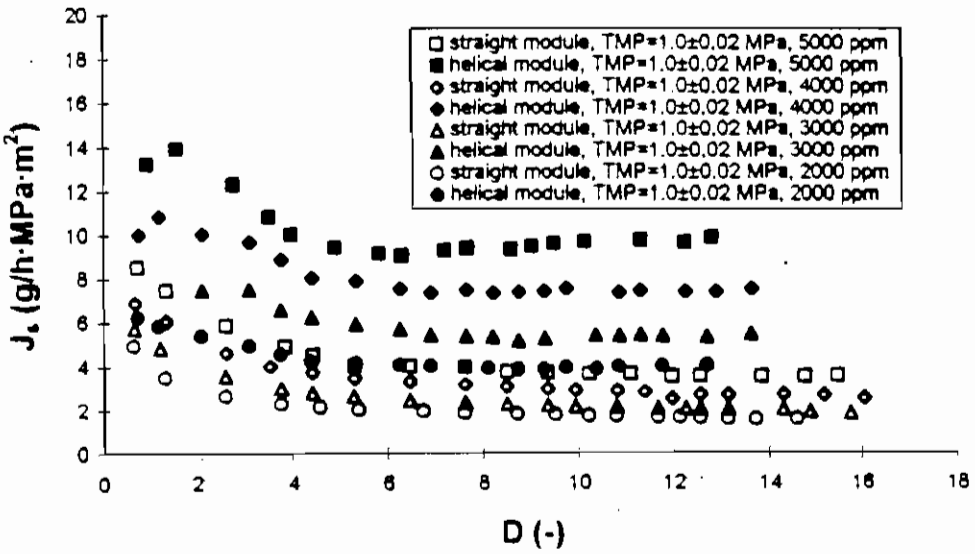

Fig. 20. Solute flux as a function of Dean number at various concentrations. TMP = 1.0 Mpa.

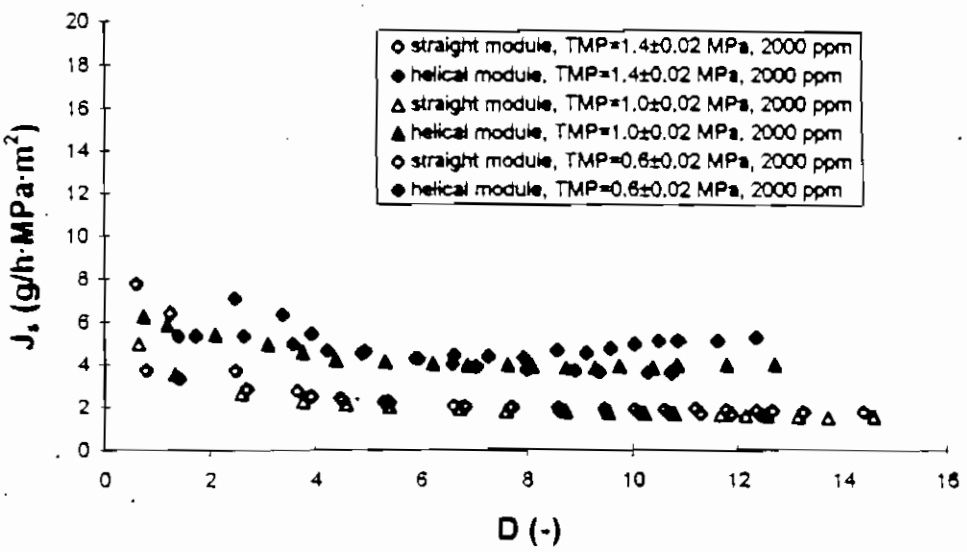

Fig. 21 (a). Solute flux as a function of Dean number at various transmembrane pressures. c = 2000 ppm.

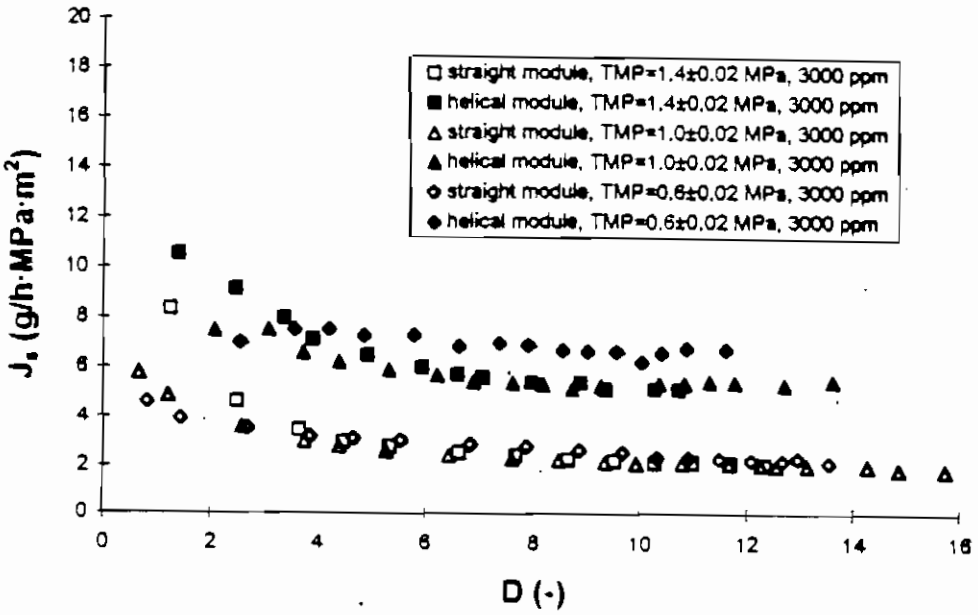

Fig. 21 (b). Solute flux as a function of Dean number at various transmembrane pressures. c = 3000 ppm.

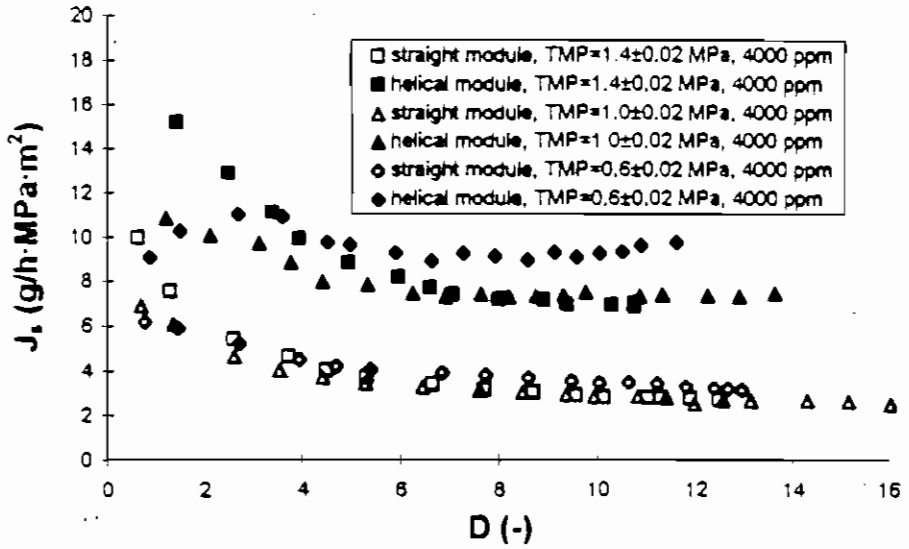

Fig. 21 (c). Solute flux as a function of Dean number at various transmembrane pressures. c = 4000 ppm.

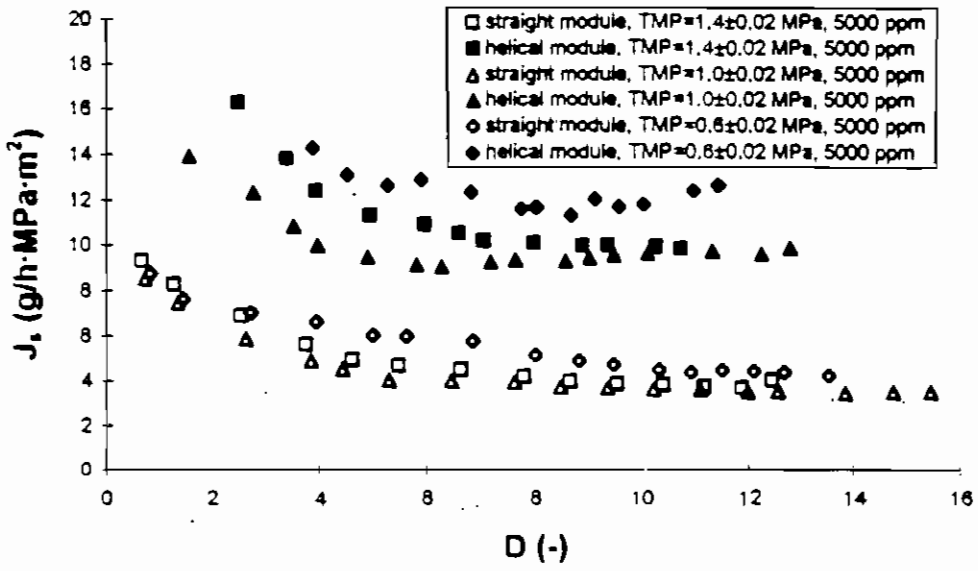

Fig. 21 (d). Solute flux as a function of Dean number at various transmembrane pressures. c = 5000 ppm.

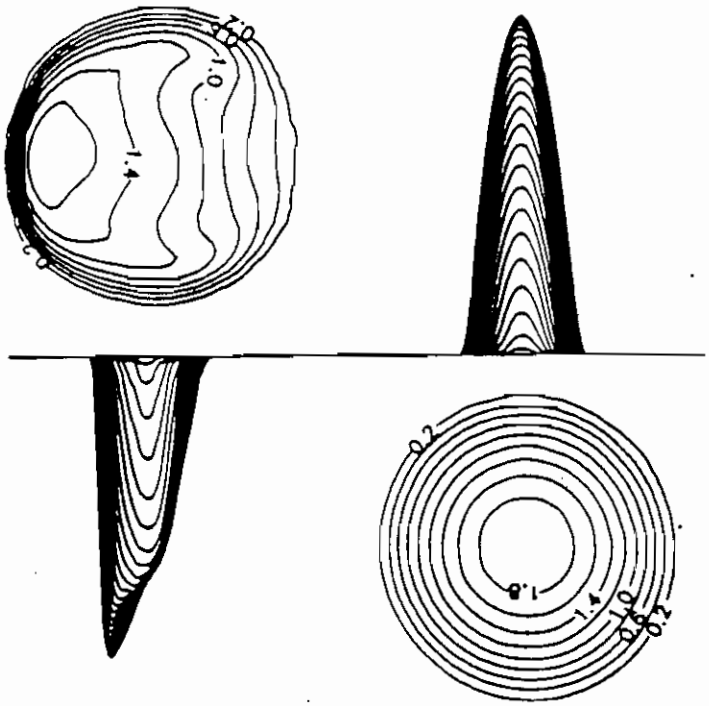

Fig. 22. Typical axial velocity profiles in a curved tube. The contours are squeezed to the left because of Dean vortices.

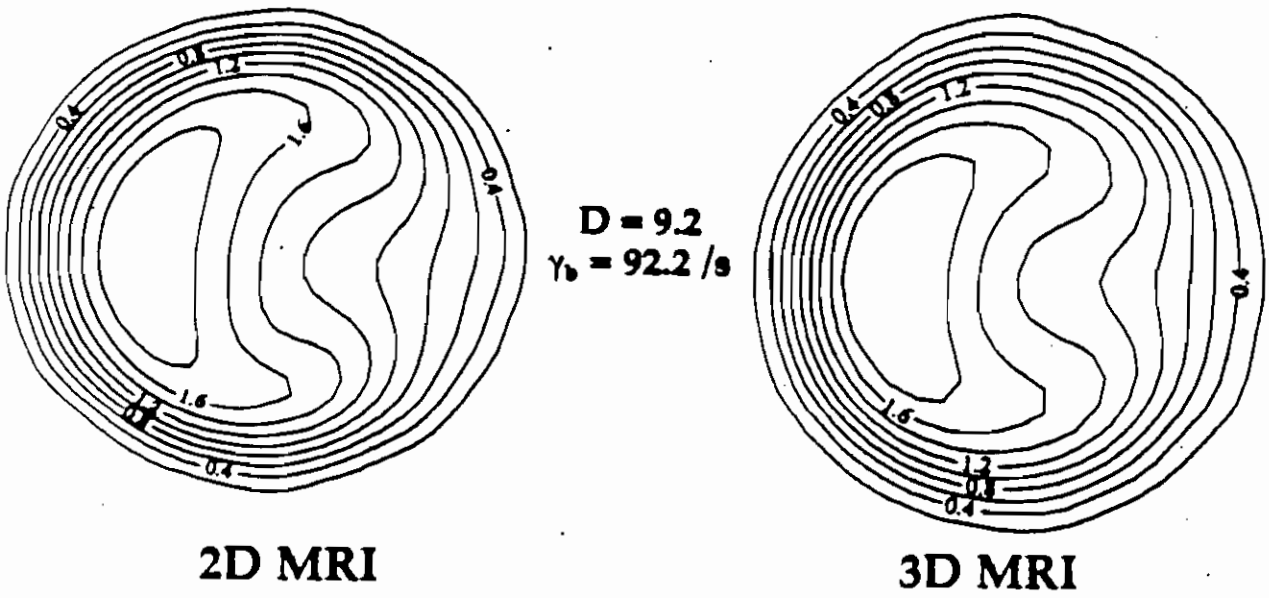

Fig. 23. Axial velocity contour profiles as obtained by 2-D and 3-D MRI. No significant difference can be seen.

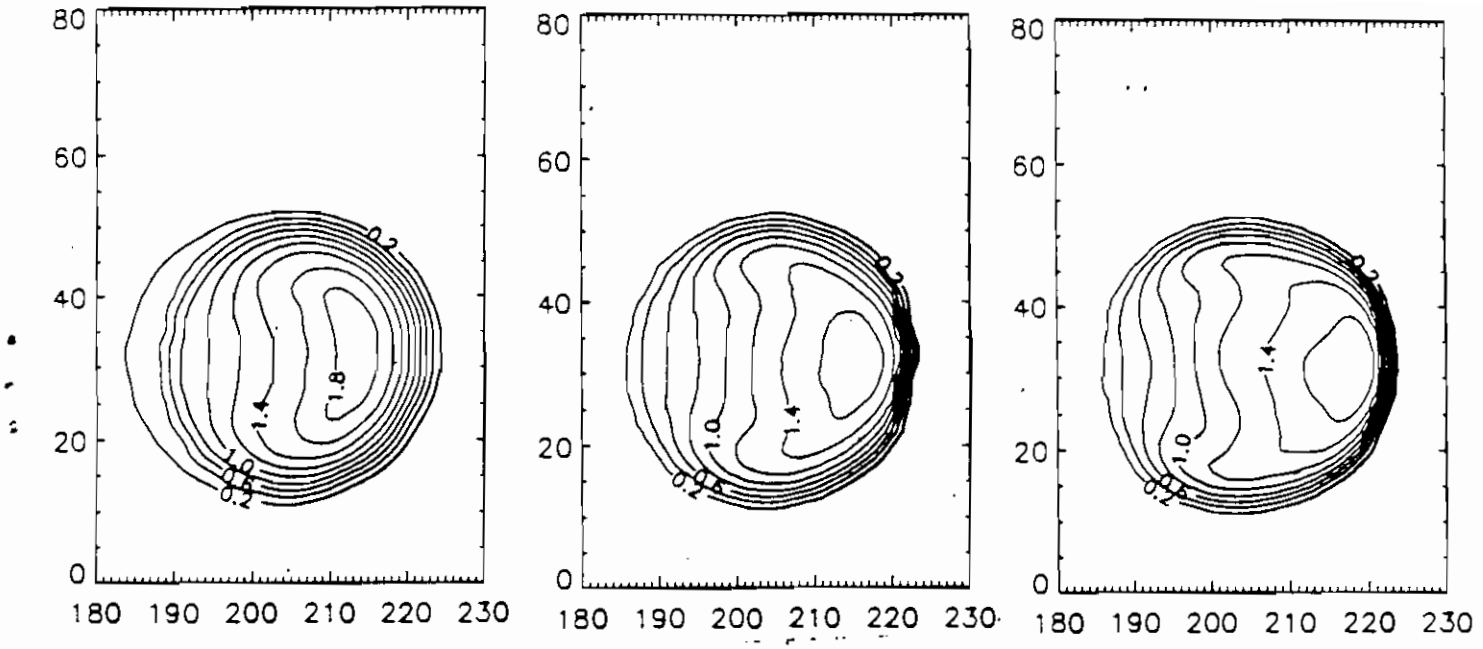

(a) De = 22.3 (b) De = 40.9 (c) De = 64.2

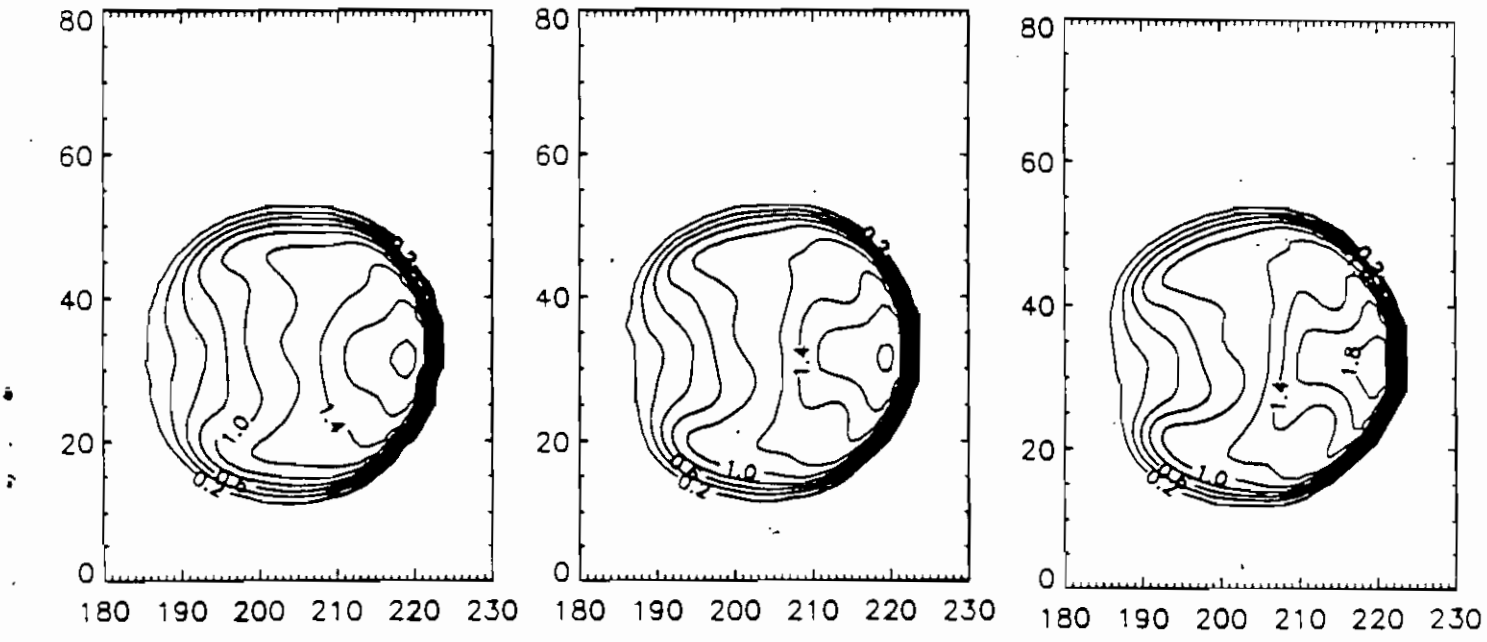

(d) De = 88.4 (e) De = 112.6 (f) De = 136.8

Fig. 24. Normalized axial velocity contour profiles in a curved tube as a function of Dean number for De = 22.3 - 275.4 [(a) - (k)]. Radius ratio, $(a/r_c) = 0.317$. $De_c = 16.4$, a = 8.02 mm.

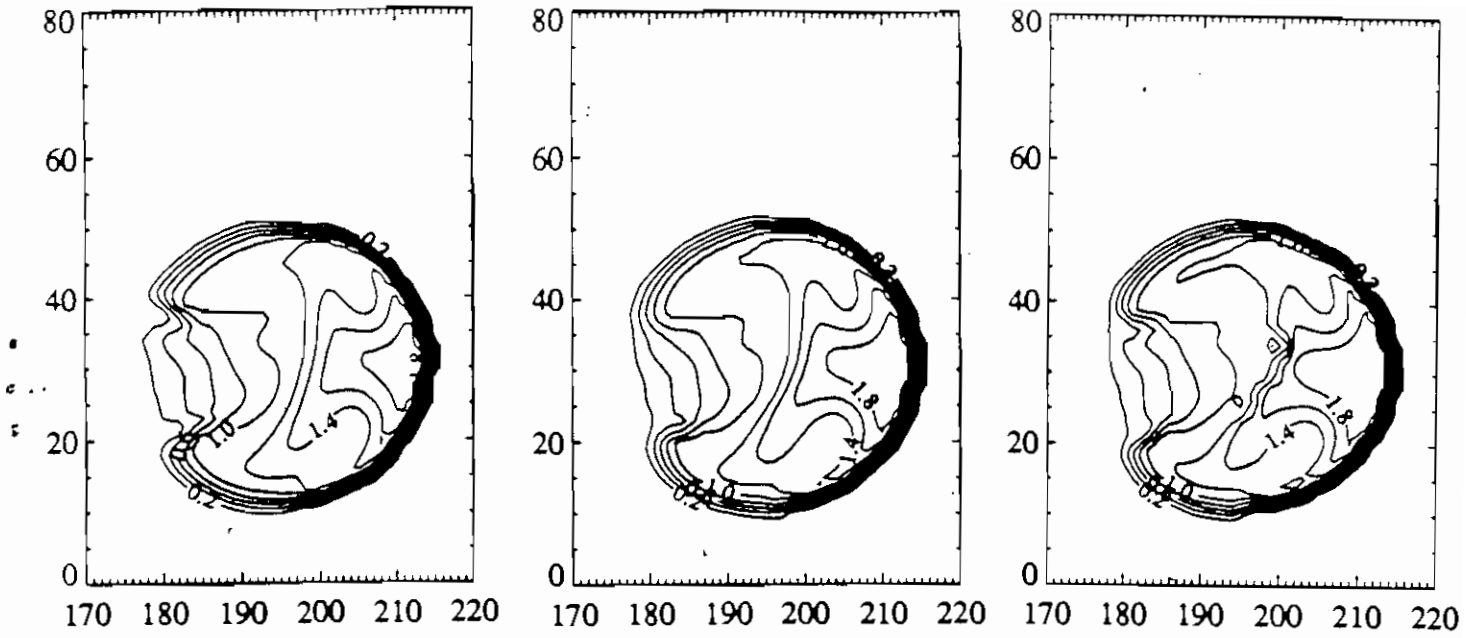

(g) De = 162.8 (h) De = 189.8 (i) De = 217.7

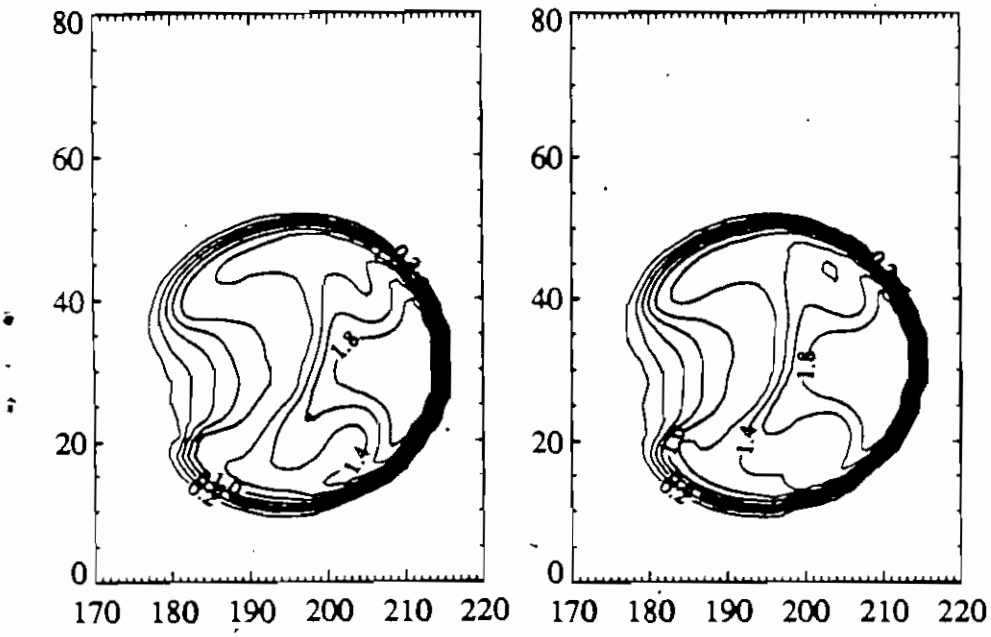

(j) De = 246.6 (k) De = 275.4

Fig. 24. Continued from previous page.

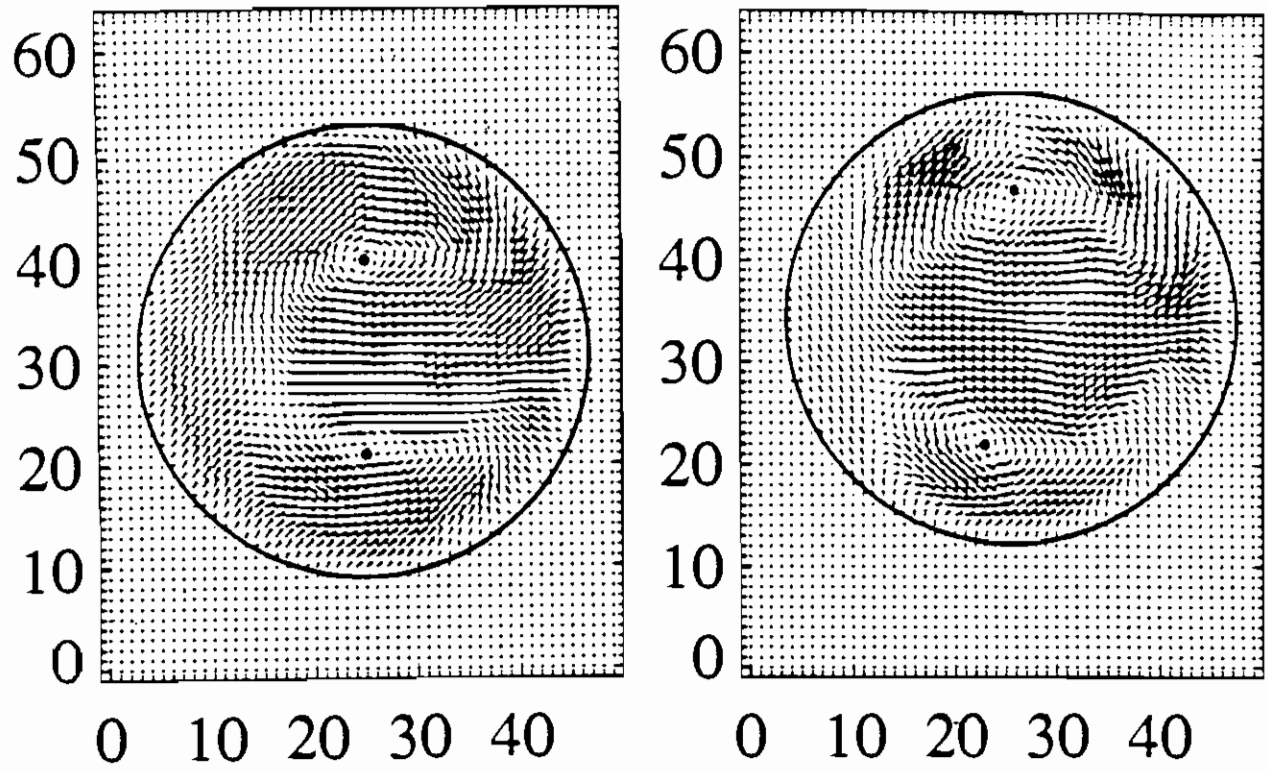

(a) De = 22.3 (b) De = 40.9

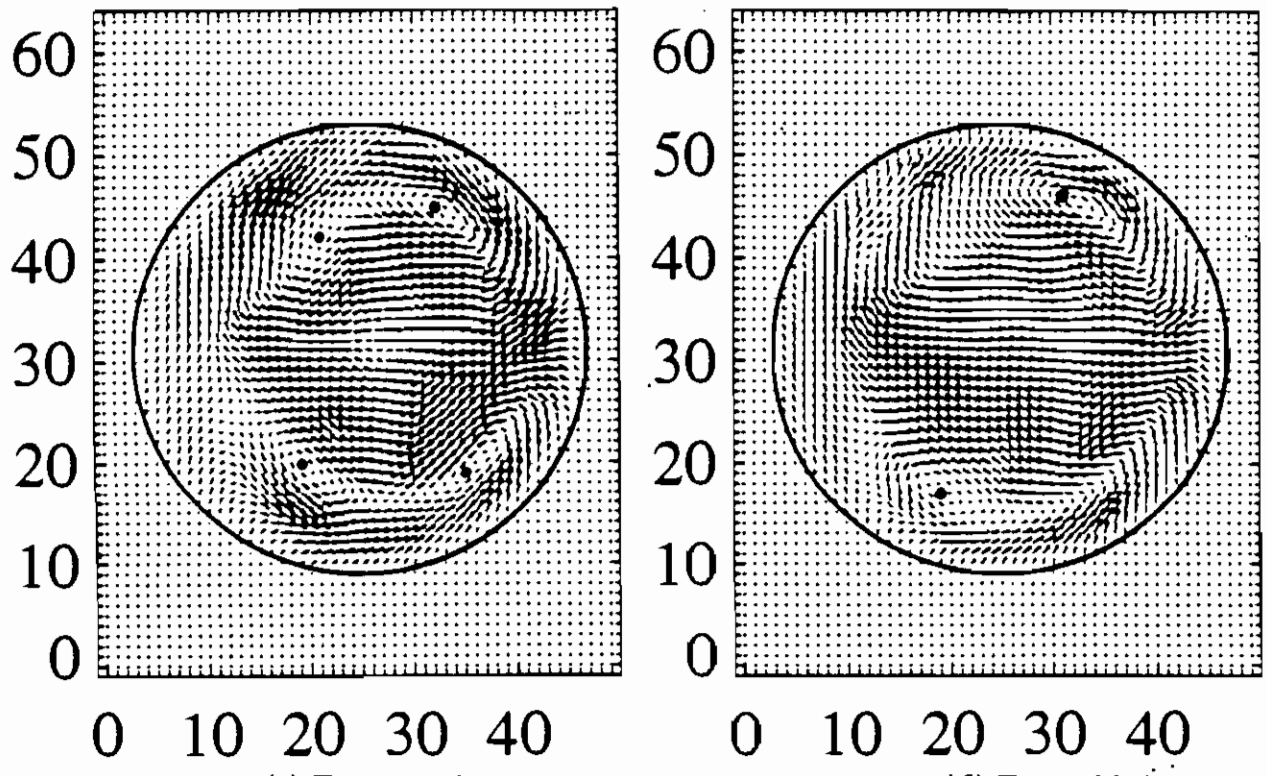

(c) De = 64.2 (d) De = 88.4

Fig. 25. Transverse velocity patterns for flow in a curved tube as a function of Dean number for water doped with cupric sulfate. $(a/r_C) = 0.317$. $De_C = 16.42$, a = 8.02 mm. $Re_C = 29.17$. (a) - (k) for De = 22.3 -275.4. Points (•) are the "eyes" of the vortices.

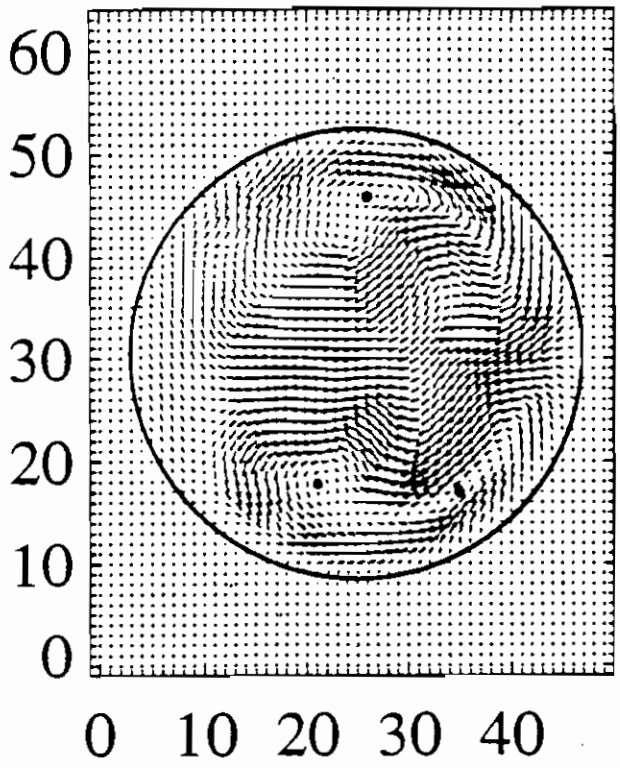

(e) De = 112.6

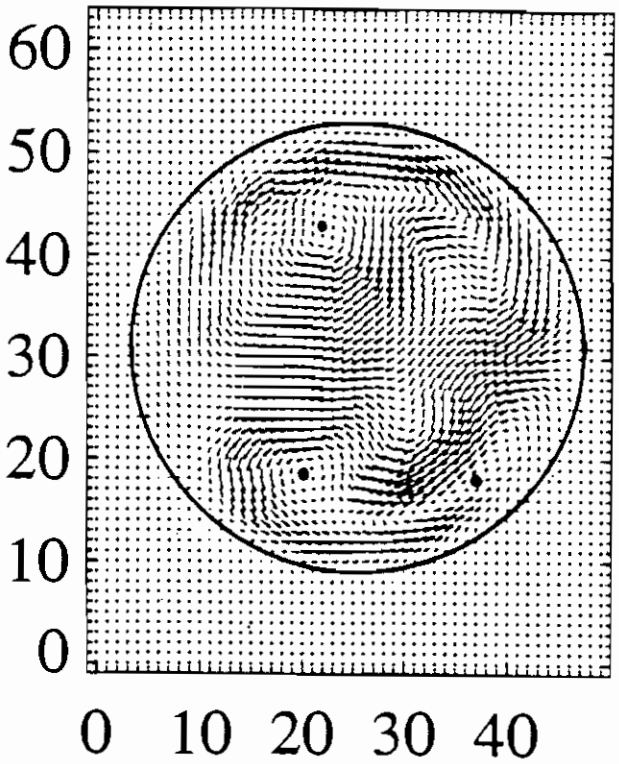

(f) De = 136.8

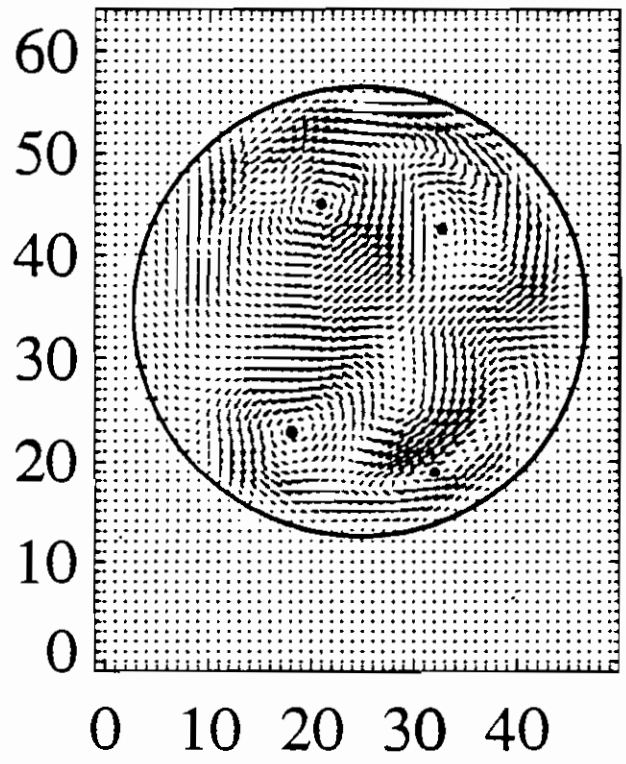

(g) De = 162.8

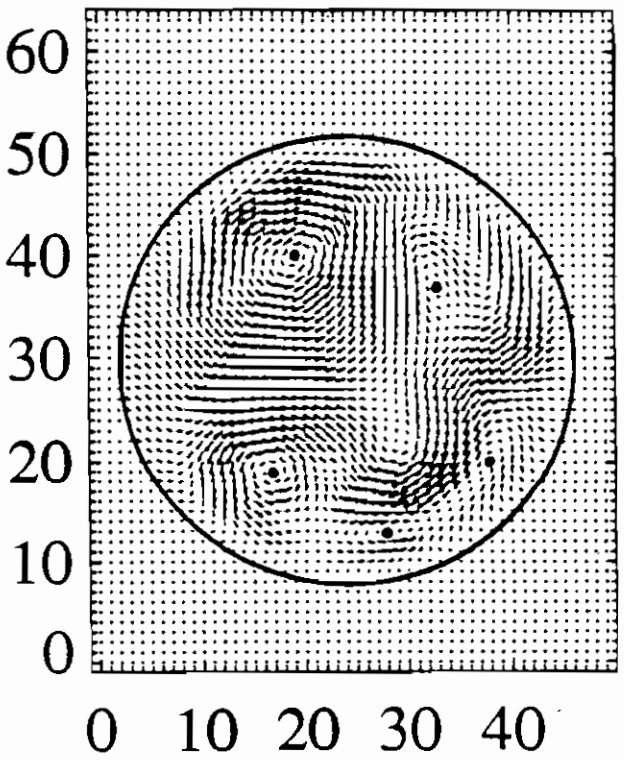

(h) De = 189.8

Fig. 25. Continued from previous page.

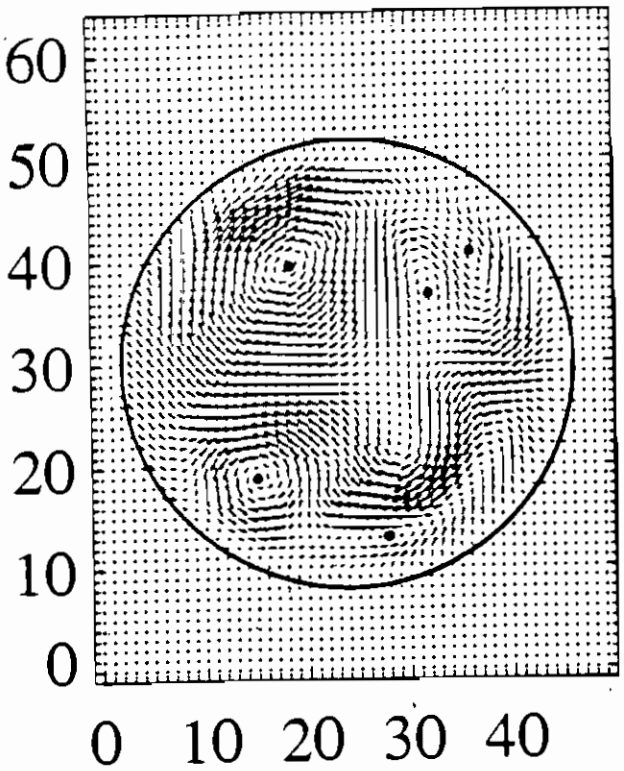

(i) De = 217.7

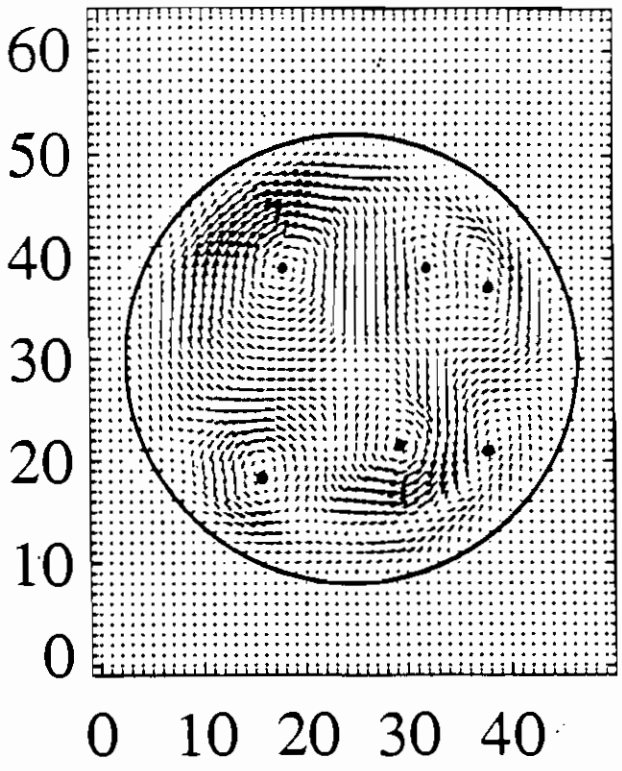

(j) De = 246.6

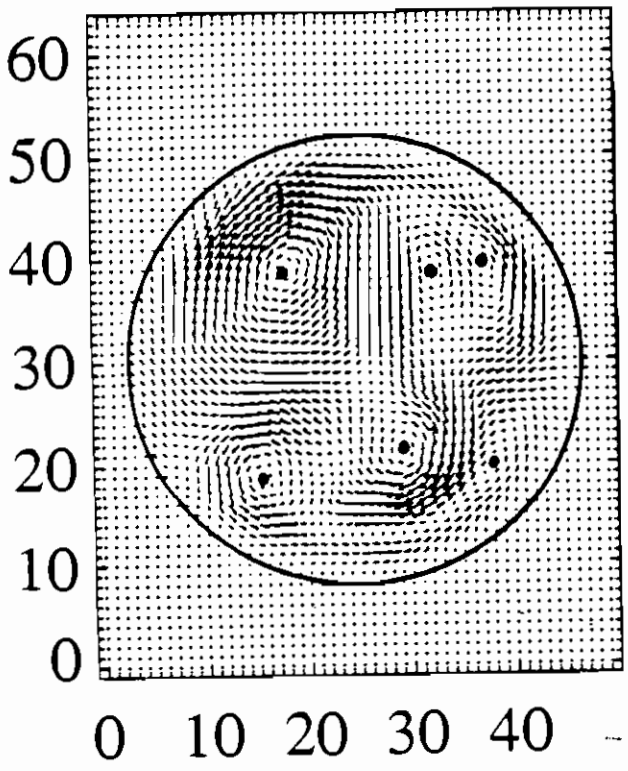

(k) De = 275.4

Fig. 25. Continued from previous page.

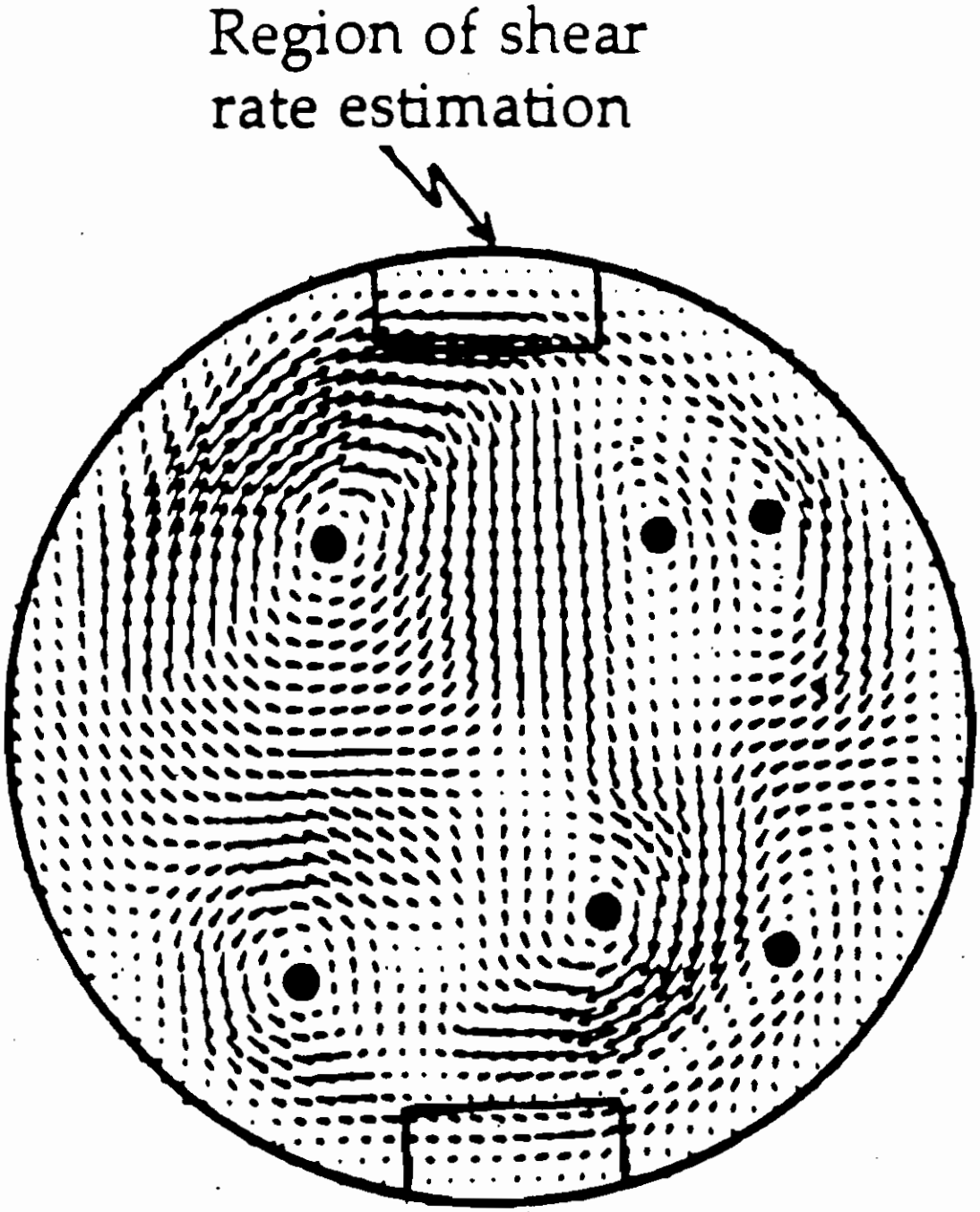

Fig. 26. Transverse velocity patterns for flow water doped with cupric sulfate, in a curved tube. $(a/r_c) = 0.317$. $De_c = 16.42$, a = 8.02 mm. $Re_c = 29.17$. The six - vortex pattern and the region of shear rate estimation.

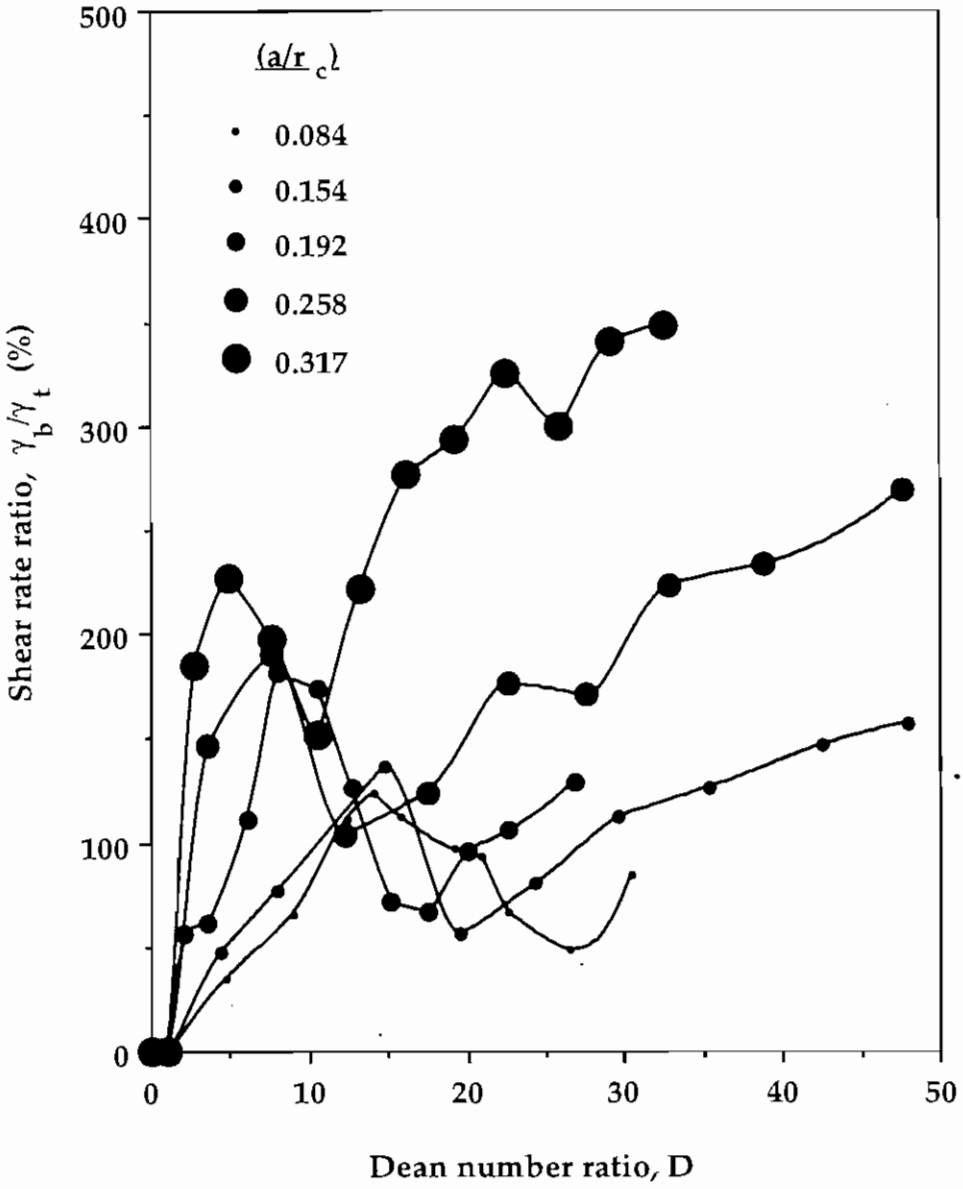

Fig. 27. Effect of radius ratio on Dean shear rate.